Detailed analysis of fringe field effects in the Large Hadron Collider

Béla Erdélyi, Martin Berz and Kyoko Makino
Department of Physics and Astronomy and
National Superconducting Cyclotron Laboratory,
Michigan State University, East Lansing, MI 48824

July 26, 1999

Abstract

We study single particle dynamics of the LHC in the map picture with emphasis on fringe field effects. Using the results of our fringe field map computation methods [1], it is rather easy to take into account in a rigorous way the influence of fringe fields. As indicators of the nonlinear dynamics we use tune footprints, tune shifts, resonance strengths and resonance webs. A total of 10 situations are studied, from the simple to the more complex. Comparisons are presented which are meant to clarify topics like: is the exact shape of fringe fields important, relative importance of individual multipole components in the fringe fields, and relative importance of fringe fields with respect to body errors.

1   Introduction

Recently, many studies have been published on single particle dynamics in the Large Hadron Collider to be built at CERN. See [2] and references therein. Specifically, at collision energy it has been shown that the dynamics is dominated by the interaction region's high gradient quadrupole triplets. This is due to large variations of the β functions across the quadrupoles. The studies concentrate on many possible realizations of the LHC lattice, that is, on computing the effects of the so-called systematic and random body errors, and perhaps other effects like crossing angle, beam-beam interaction, misalignment, etc. The fringe fields, traditionally, are taken into account at most at the level of lumped thin lenses (kicks), characterized by integrated multipole strengths. However, it is not obvious whether this simplistic approach is enough to give an accurate account of the dynamics under the influence of fringe fields. The present paper attempts to fill this gap by assessing the impact of fringe fields via very accurate fringe field maps, at least for the LHC, and specifically for the low-β insertion quadrupoles.

The studies contained in the present paper are the follow-up of our results on Differential Algebraic field computation. We showed in [1] how to take into account the local structure of s-dependent fields, resulting in the computation of very accurate fringe field maps. We use the fringe field maps computed with the methods of [1] to study systematically their effect on the nonlinear dynamics of the LHC. Starting from the ideal lattice, we gradually include more and more effects and study their influence measured by tune-shifts, resonance strengths and sometimes resonance webs. We keep an eye on the importance of the exact shape of fringe fields and relative importance with respect to body errors. Results concerning off-energy particles are included too.

2   Methods of analysis

We use as measures for the dynamics indicators that have been proven effective in predicting the performance of existing accelerators, and were useful for construction of correction schemes for proposed machines. We will employ tune footprint, tune shift, resonance strength and resonance web calculations. All of them are based on normal forms of symplectic maps. We assume that the LHC is accurately described by the n-th order Taylor expansion of the system's true map, $\mathcal{M}$. Because hadron accelerators can be regarded as large Hamiltonian systems, the truncated map will be symplectic to order n. It means that relative to some symplectic coordinates $\vec{z}$ its Jacobian, M, satisfies the symplectic condition to order n

$$M^T J M = J. \tag{1}$$

The truncated map can be subjected to an order by order symplectic change of variables that finally yields its normal form. That is, there exist symplectic maps $\mathcal{A}_n$ such that

$$\mathcal{N} = \mathcal{A}_n \circ \mathcal{M} \circ \mathcal{A}_n^{-1}, \tag{2}$$

The symplectic map $\mathcal{N}$ takes a particularly simple interpretation; it is a rotation with radius dependent frequency. See [3] for details. The angles of advancement of a point on a torus after one application of the map are called the tunes of the respective particle. Its deviation from the tune of a particle with 0 amplitude (the linear tune) is called the tune-shift. Due to the fact that the normal form of a symplectic map is unique, also the tune-shifts are uniquely defined. We compute these quantities for the various cases studied. In general, for good performance of accelerators, large tune-shifts are to be avoided.

In this setting, the resonance condition is defined as

$$\vec{k} \cdot \vec{\mu}\left(\vec{J}, \vec{\delta}\right) = m \pmod{2\pi}, \tag{3}$$

for a vector of integers $\vec{k}$ and integer m. The tunes are denoted by $\vec{\mu}$, $\vec{J}$ represents the action variables (the radii), and $\vec{\delta}$ the parameters. Although the normal

form transformation can be used to compute the tunes only in the non-resonant case, it is our hope that extrapolation of the results close to the resonant case can give insight into the dynamics of resonant orbits. For this purpose we study eq. 3 as a function of $\vec{J}$. By adding to the right hand side a small quantity $\varepsilon \ll 1$, with fixed maximum value, we plot in action space the $\vec{J}$'s that satisfy the resonant condition. This gives insight into the resonance orbit structure of the phase space directly. This picture of the location and width of resonance lines is called the resonance web. The intuitive interpretation of the role of ε is that it translates a fixed, small distance in tune space around exactly resonant orbits into oscillation of the action variables around exactly resonant orbits. The amount of oscillation gives a measure of the width of the resonance lines. Overlapping of resonance lines are considered signs of chaos, which is not necessarily bad in theory, but in practice usually it is. Often, the dynamic aperture is close to the chaotic boundary. Hence, the closeness of the resonance lines to the origin in action space again can be a useful indicator.

It is not easy to explain the method of computing the resonance strengths without getting into unnecessary details. This is partly due to the fact that the resonance strengths are not defined uniquely. Usually it is based on the normalizing map, $\mathcal{A}_n$, which is known to not be unique. Moreover, the manipulation of the elements of $\mathcal{A}_n$ is somewhat arbitrary. Anyway, as a general rule, the resonance strengths are directly proportional to the nonlinearity of the underlying map and its distance from resonances, measured by the resonance denominators, which are the left hand sides of eq. 3. For more details of a method similar in spirit to our calculation we refer the reader to [4]. The difference between the two methods is that we do not use Lie algebraic techniques, but we work directly with the Taylor expansions of the components of the normalizing map. Despite all this, the correction of dominating resonances proved to be an effective tool for improving the performance of accelerators. We could say, that although the exact numerical values of the resonance strengths do not really have relevance (as they are method dependent), the qualitative picture it is useful (for example identifying the dominating resonances).

We mention that none of the above indicators have an absolute correlation with the behavior of particles in accelerators. In some cases one of them can have a better correlation with the dynamic aperture, in other cases another indicator, or none. However, altogether probably they can reveal the gross features of the dynamics, and can be useful in practice.

3   Cases studied

All maps, fringe field and rest of the lattice (LHC v.5.1), have been computed at order 8 using the code COSY Infinity [5]. Due to sensitivity to numerical errors, especially at high orders, of the tune-shift computation and occurrence of large numbers in the maps, we performed all the calculations in quadruple precision. The effects of RF cavities have been neglected, i.e. we computed the maps in two transversal degrees of freedom, with energy

as a parameter. At the specific location of the lattice where we fixed the Poincare section, the r.m.s. beam sizes are $\sigma_x = 1.267 \cdot 10^{-4} m$ and $\sigma_y = 2.981 \cdot 10^{-4} m$. It is also known from the design specifications that the r.m.s. normalized emittance is $\varepsilon_N = 3.75 \cdot 10^{-6} m \cdot r$ and the r.m.s. energy deviation is $\sigma_E = 1.1 \cdot 10^{-4}$. For body errors we used the Table MQXB (FNAL High Gradient Quad) Reference Harmonics at Collision v. 2.0, available on the WWW at the address http://www.agsrhichome.bnl.gov/LHC/fnal/v2.0/hgq_col_v2p0.txt. The detailed analysis of the body errors where not the main purpose of our studies, so we used only one seed for the random body errors, which gives "average" results in some sense (for example dynamic aperture). For the systematic part of the errors we employed their full uncertainty, with the two possible signs. That is, if we denote by $\langle b_n \rangle$ the average value of a multipole, then the multipole value due to uncertainty lies between $-d(b_n) + \langle b_n \rangle \le b_n \le +d(b_n) + \langle b_n \rangle$. Hereafter we will refer to the two cases of full uncertainty by their sign, $(-)$ or $(+)$.

To assess the importance of fringe field shape, we use two different models. One is the "detailed" shape, based on the exact shape of the fringe field computed using the model HGQS01 [6]. The other is a "default" fringe field shape, as implemented in the code COSY Infinity, based on the fall-off modeled by an Enge function [5]. The detailed fringe fields detune the ideal lattice and also introduce linear coupling between the planes. To obtain meaningful results we have to retune and decouple the lattice. We achieve this in a rather elegant way using an ideal local correction. Moreover, the method provides a way to keep the design linear lattice completely unchanged. It is done by splitting the fringe field maps in two parts

$$M_{ff} = L_{ff} + N_{ff}, \tag{4}$$

where L_{ff} is the linear part and N_{ff} is the nonlinear part. Application of the inverse of the linear map, which can be thought of as the zero length insertion ideal local corrector, we obtain for the fringe field map

$$\tilde{M}_{ff} = I + L_{ff}^{-1} \circ N_{ff}, \tag{5}$$

where I is the identity map. The identity as linear part ensures that the linear layout of the lattice remains unchanged. Of course, we would get a slightly different result if we were to apply L_{ff}^{-1} from the right. However, L_{ff} is close to identity, so L_{ff}^{-1} is also close to identity, and hence almost commutes with the nonlinear part. Again, this is an ideal case, and it is very likely that any real world correction scheme would introduce more nonlinearities in the map of the system. As a final remark, we mention that it is enough to compute only the exit focusing fringe field maps, and obtain the other variants by mirroring operations and rotations. Also, we use the same symmetry based tricks to get the correct maps for the proposed layout of the interaction regions, which includes rotations of quadrupoles around their vertical axis. The respective procedures are described in Appendix A.

CASE	SYSTEM
1	Interaction regions at order 8, rest linear Fringe fields and body errors OFF
2	Interaction regions at order 8, rest linear HGQ detailed fringe fields ON
3	Interaction regions at order 8, rest linear Only quadrupole components of HGQ fringe fields ON
4	Interaction regions at order 8, rest linear HGQ default fringe fields ON
5	Whole lattice at order 8 Fringe fields and body errors OFF
6	Whole lattice at order 8 detailed fringe fields for HGQ, and default fringe fields for rest of ring ON; body errors OFF
7	Whole lattice at order 8 fringe fields OFF, body errors ($-$) ON
8	Whole lattice at order 8 fringe fields OFF, body errors ($+$) ON
9	Whole lattice at order 8 fringe fields from case 6 ON, and body errors ($-$) ON
10	Whole lattice at order 8 fringe fields from case 6 ON, and body errors ($+$) ON

Table 1: The various cases studied.

Table 1 contains all the cases studied, starting from the simple to the more complex.

In the following section we describe the results obtained for each of them. We will refer to the specific case by their number in the table.

4 Results and discussion

The results shed light on the relative importance of intrinsic nonlinearities of the ideal lattice, the fringe field induced nonlinearities, and body errors induced nonlinearities. The tunes are visualized in two different ways. The $2d$ pictures represent the usual tune footprint style, and the $3d$ pictures show the tune shift of particles as a function of initial amplitudes in geometric space, in units of r.m.s. beam sizes, up to 6σ. The tune-shifts in the $3d$ pictures are all in units of 10^{-4}. The resonance strengths are computed close to the expected dynamic aperture, along the diagonal in action space. The units are arbitrary, and we denote $\vec{k} = (q, p)$. Also, for cases 9 and 10 we computed the resonance strengths on a grid of points to identify the dominating resonances in different locations of phase space. Every case is subdivided in 3 subcases according to energy: $\delta = -2.5\sigma_E, 0, +2.5\sigma_E$. For the computation of resonance webs we used a

maximum value of $\varepsilon = 10^{-3}$. The size of the beam at the expected dynamic aperture is approximately $J_x = J_y = 5 \cdot 10^{-4} m$.

Let us start with the first, most simple case. Case 1 represents the linear LHC lattice with only the intrinsic nonlinearities of the interaction region quadrupoles added. As we expected, figures 1, 2 and 3 show that the nonlinearities are insignificant.

The tune footprints have regular shapes, but practically vanishing size. For off-energy particles the dominating resonance is $(2, 0)$, which is 2 orders of magnitude bigger than the dominating resonance for on-energy particles, $(2, -2)$.

Case 2 is actually case 1, to which we add the detailed fringe fields of the High Gradient Quadrupoles of the interaction regions. The acceptance guidelines require a tune shift of less than 10^{-3} at 6σ.

We can see that the nonlinearities introduced by the fringe fields are considerable. See figures 4, 5 and 6. However, tune shifts are still inside the safe region. Also, the tune footprints get bigger and have highly irregular shapes. Maximum values of tune shifts and size of tune footprints decrease as the energy increases. The sharpest decrease with energy is experienced by particles with small initial y and large initial x. Dominating resonances are the $(2, -2)$, also encountered in case 1, and a newly excited resonance, the $(1, -1)$. There is an increase in the absolute values of the resonance strengths, compared with case 1. The resonances are almost invariant with respect to energy. Also, their magnitudes are slightly increasing with energy, an opposite tendency when compared to tune shifts.

Next, we studied what is the relative importance of only the quadrupole components. Therefore, case 3 is case 2 without the sextupole components in the fringe fields. For the result see figures 7, 8 and 9.

We notice a 5 times decrease for the maximum tune shift for negative energy dispersion particles, and some more modest decreases for the other particles. The tune footprints are becoming a little bit smaller and regular, triangle shaped, hence the irregularities of case 2 are caused by the sextupole components in the fringe fields. Overall, the importance of the sextupole components are decreasing as the energy increases. There are noticeable differences between resonance strengths of cases 3 and 2. The magnitudes drop by 2 orders of magnitude, and become comparable with off-energy particle's resonance strengths of case 1. Moreover, they are not invariant anymore with respect to energy. While the dominating resonance, regardless of energy, is $(2, -2)$, which we carried along since case 1, again $(2, 0)$ from case 1 makes its appearance for off-energy particles, and $(1, -1)$ completely disappears. We conclude that the intrinsic nonlinearities of the quadrupoles excite the $(2, 0)$ and $(2, -2)$ resonances, all components of the fringe fields contribute to the $(2, -2)$ resonance, making it the dominating one, and the $(1, -1)$ resonance is excited only by the sextupole components, which is comparable in magnitude with $(2, -2)$. The magnitudes of the resonance strengths keep they slightly increasing behavior with energy.

Now we turn our attention to the question of the exact shape of the fringe fields. For easy comparison we created case 4, which is case 3 with the detailed fringe fields, containing only the quadrupole components, replaced by a
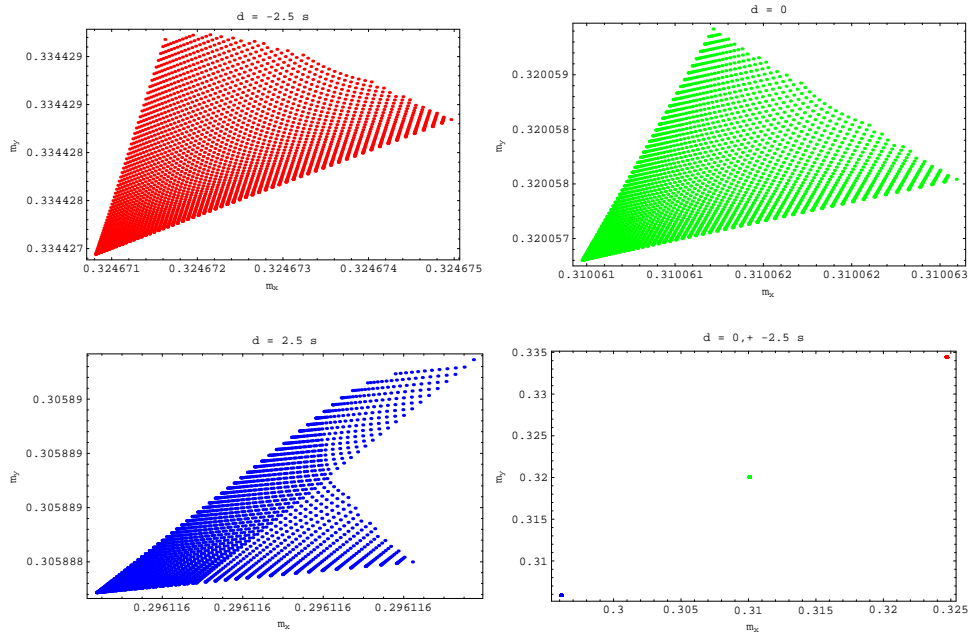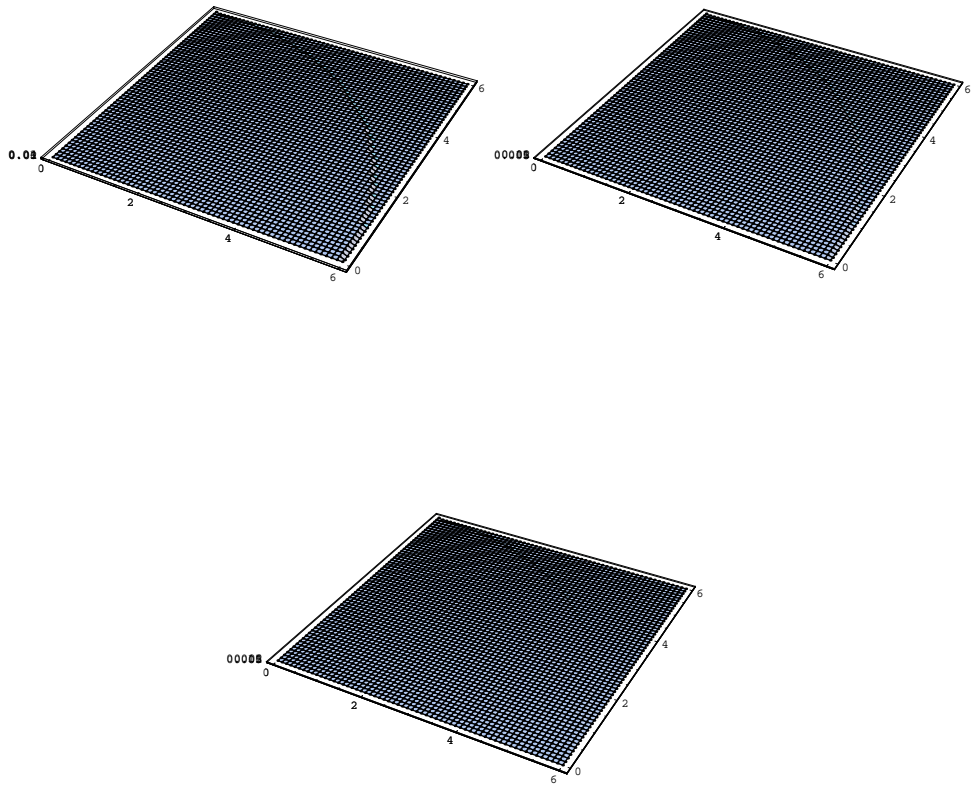
Figure 1: Tune footprints for case 1.

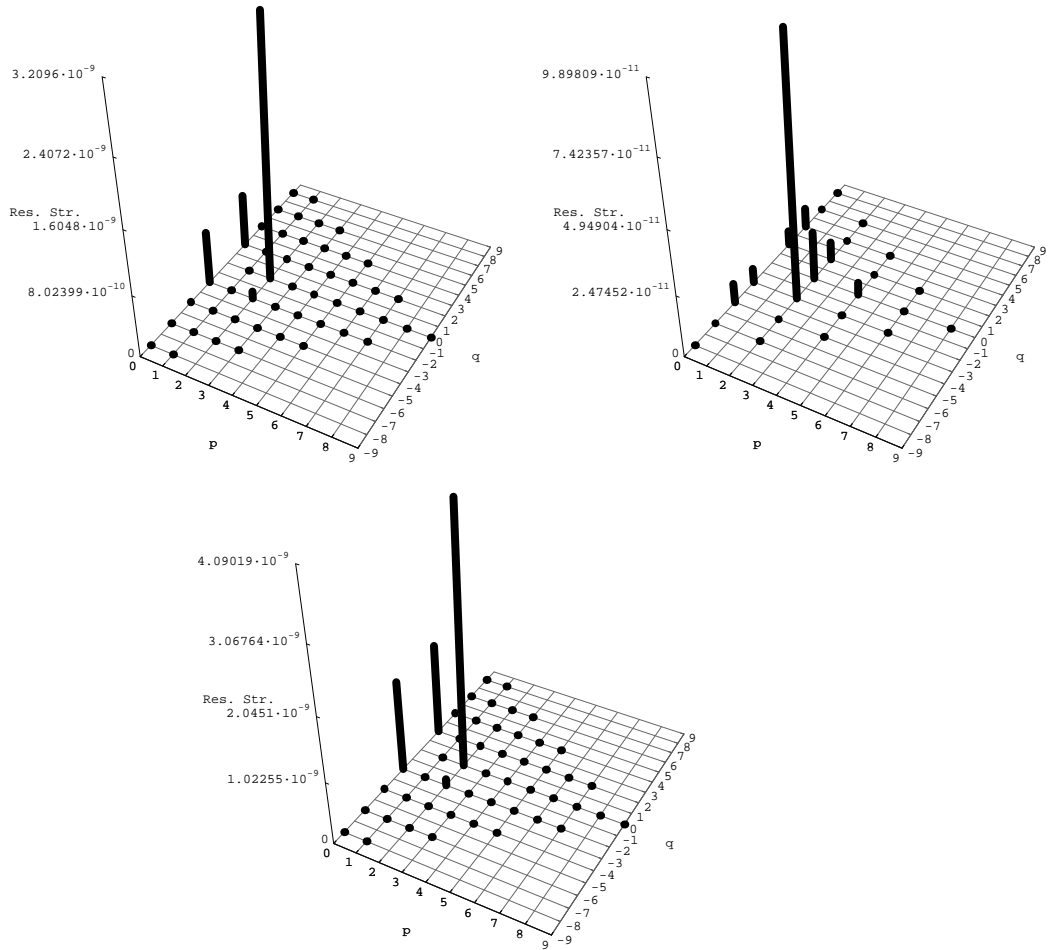Figure 2: Tune shifts for case 1.

Figure 3: Resonance strengths for case 1.

generic fringe field shape, that has a fall-off modeled by an Enge function with 6 parameters.

As one can see, the differences between the set of figures of case 3, figures 7, 8 and 9, and the figures of case 4, figures 10, 11 and 12, are marginal. The pictures are almost identical, with a small decrease in all the indicators for the generic fringe field. We conclude that, at least for the main component of the fringe fields, the exact shape is not critical.

As the next step, we studied the nonlinearities of the ideal lattice, that is no errors at all, only the intrinsic nonlinearities of the whole ring up to order 8.

8
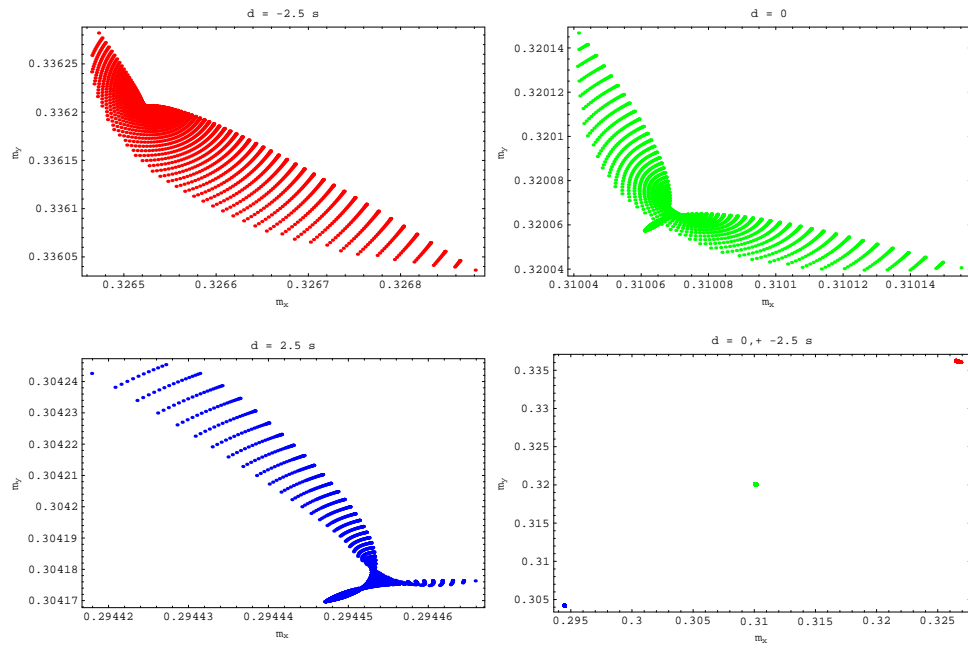
Figure 4: Tune footprints for case 2.

Figure 5: Tune shifts for case 2.
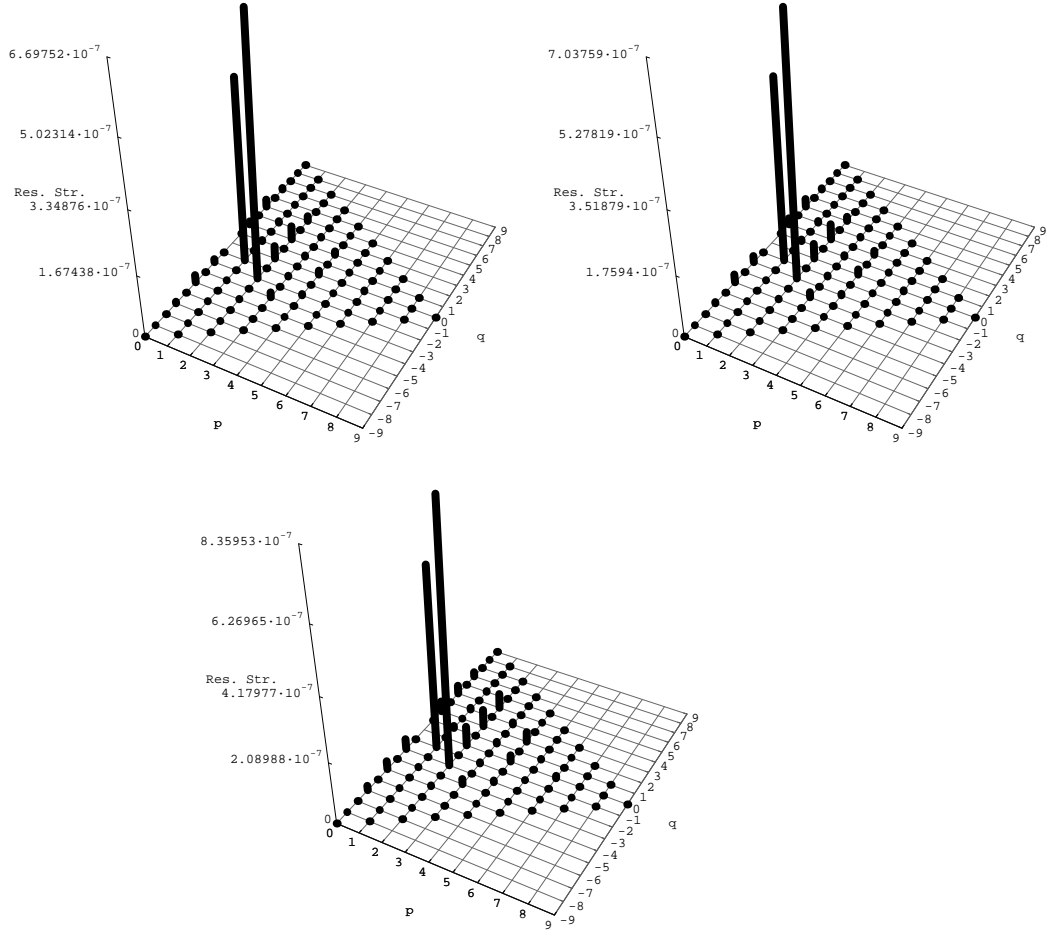
Figure 6: Resonance strengths for case 2.

This is case 5, and the relevant figures are 13, 14, 15 and 16.

The effects of the intrinsic nonlinearities of the whole lattice are comparable with those created by the fringe fields of the interaction regions. In the case of $\delta < 0$ the fringe fields cause a bigger maximum tune-shift, while for $\delta \geq 0$ the intrinsic nonlinearities are marginally bigger. Also, the tune footprints are roughly the same, but in this case the shapes are regular, triangle shaped. However, the resonance strengths are more than one order of magnitude smaller than in case 2, and they are almost invariant with respect to energy. Many more resonances are excited than sofar, with $(2, -2)$ remaining the dominant
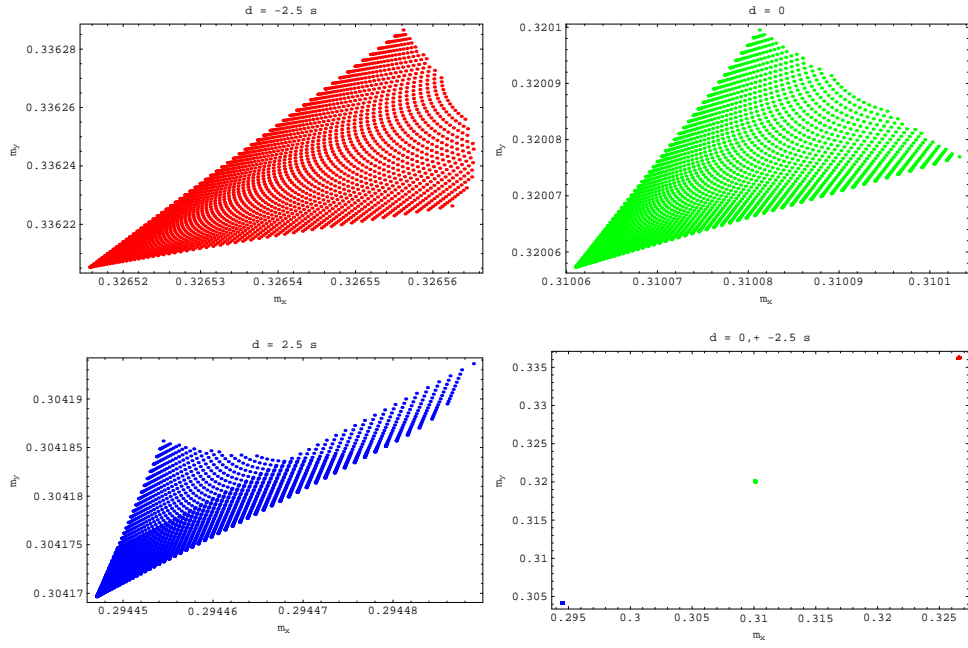
Figure 7: Tune footprints for case 3.
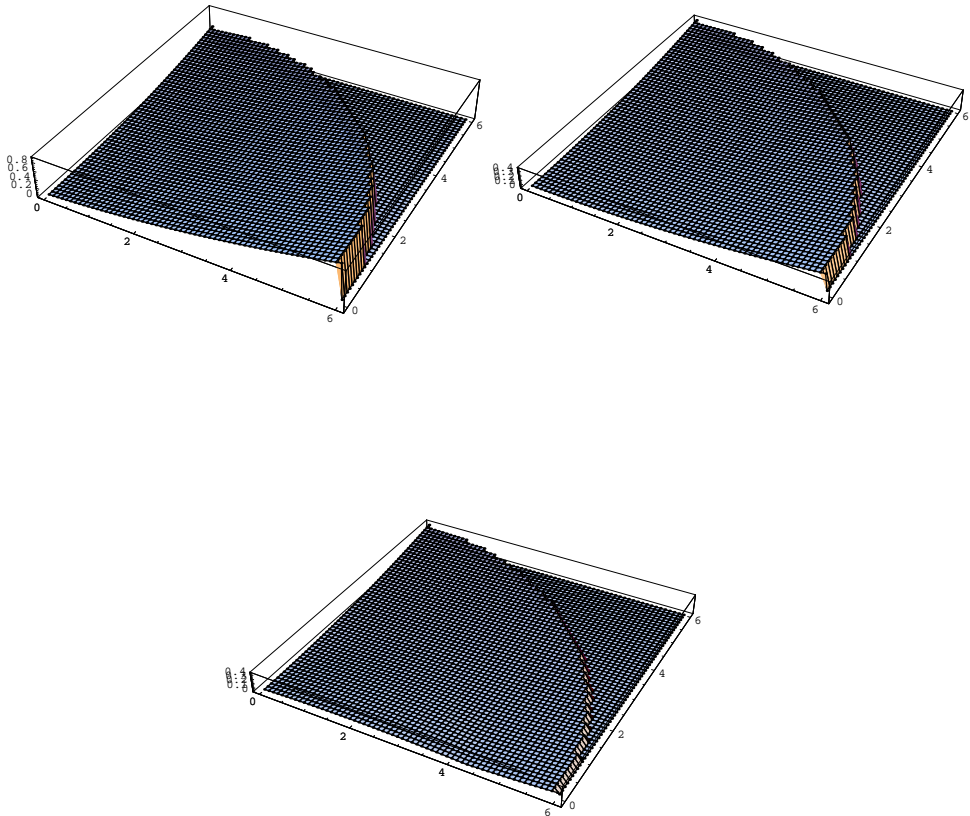
Figure 8: Tune shifts for case 3.
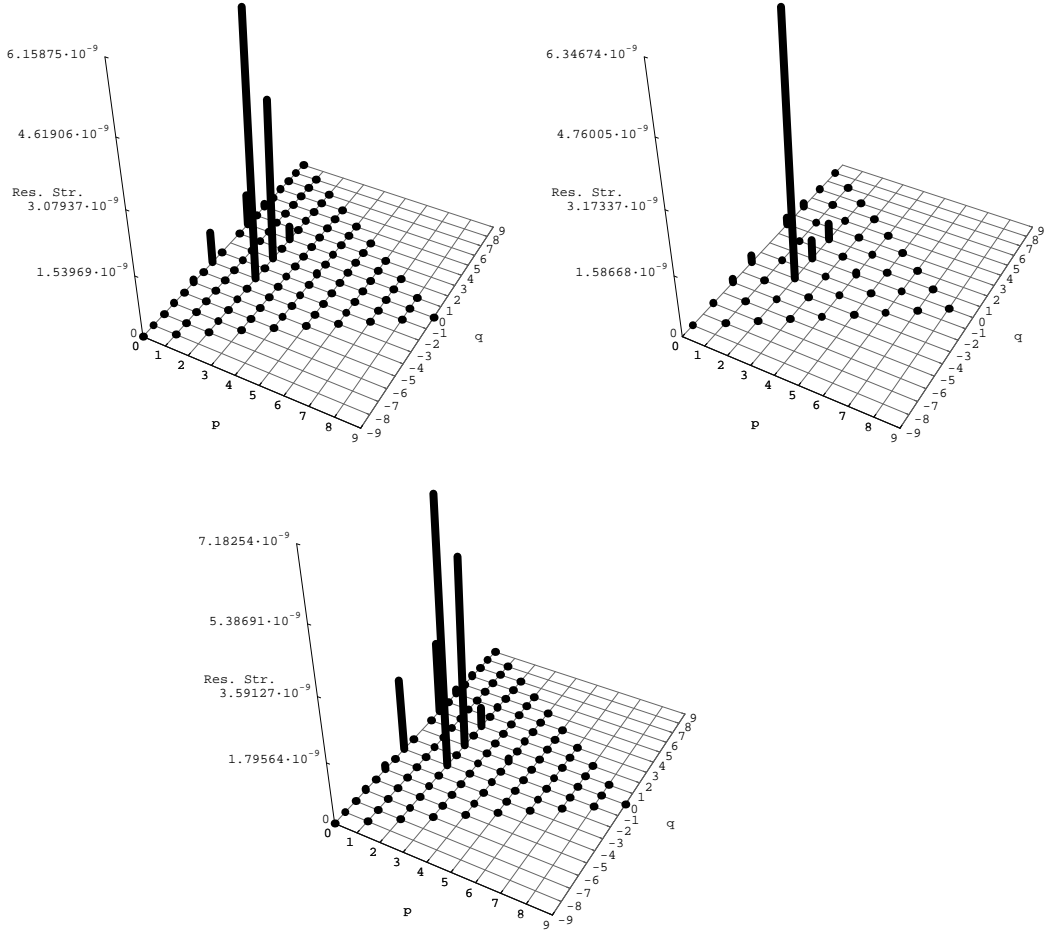
Figure 9: Resonance strengths for case 3.

one. Other excited resonances are $(1, 2)$, $(1, 0)$ and a few smaller: $(1, -2)$, $(3, 0)$ and $(2, 0)$. The $(2, 0)$ is almost completely missing for $\delta = 0$, hence it is excited mostly by off-energy particles. The resonance web shows the chaotic boundary to be at approximately $3 \cdot 10^{-3} m$. A beam of $\simeq 12\sigma_{x,y}$ occupies $\simeq 4 - 5 \cdot 10^{-4} m$ in this picture, therefore this region is completely free of low order resonances. We estimated the following resonances to be the "thickest", in decreasing order: $(1, -1)$, $(2, -2)$, $(3, -3)$, $(4, -4)$, $(6, 1)$ and $(8, -1)$.

Case 6 represents case 2 and case 5 superimposed, and additionally generic fringe fields are set on for the remaining of the ring.
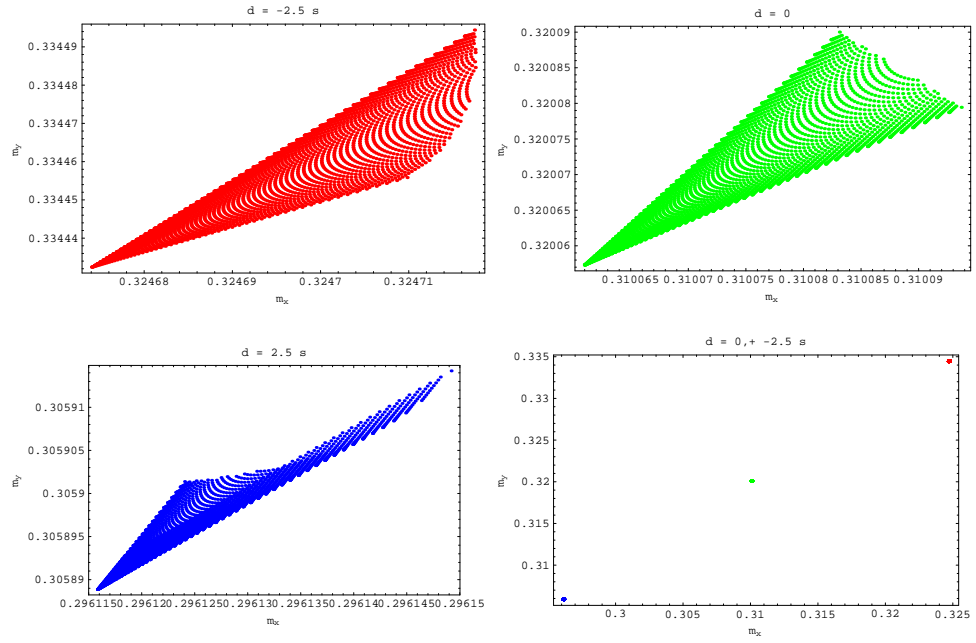
Figure 10: Tune footprints for case 4.
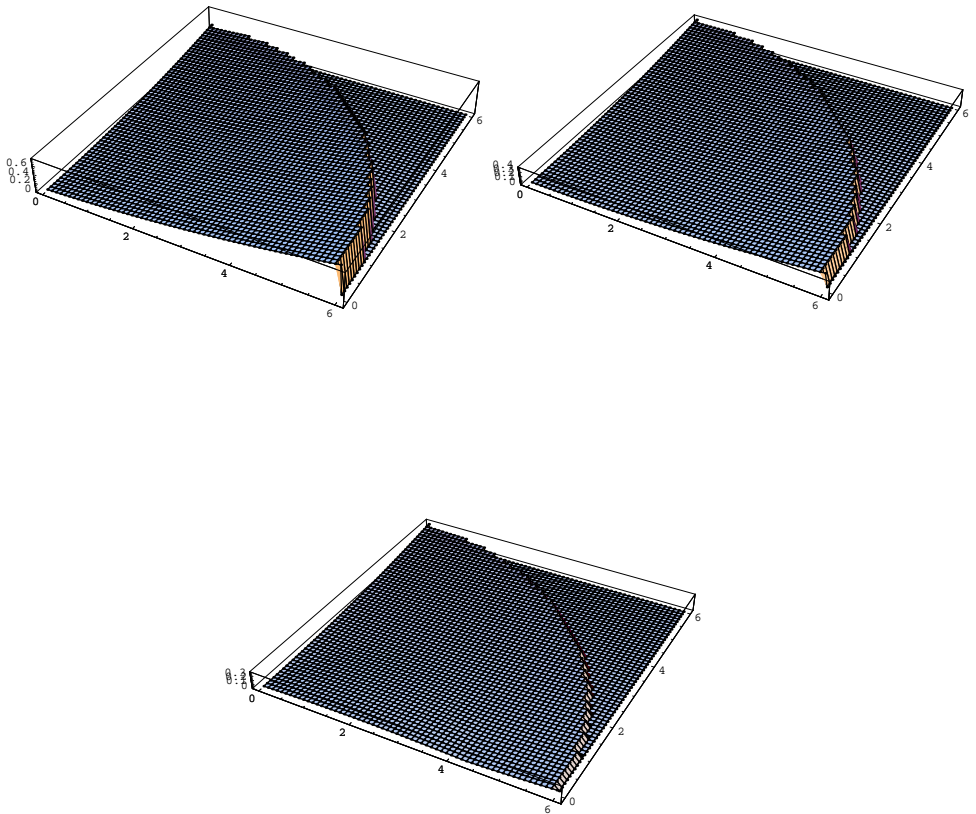
Figure 11: Tune shifts for case 4.
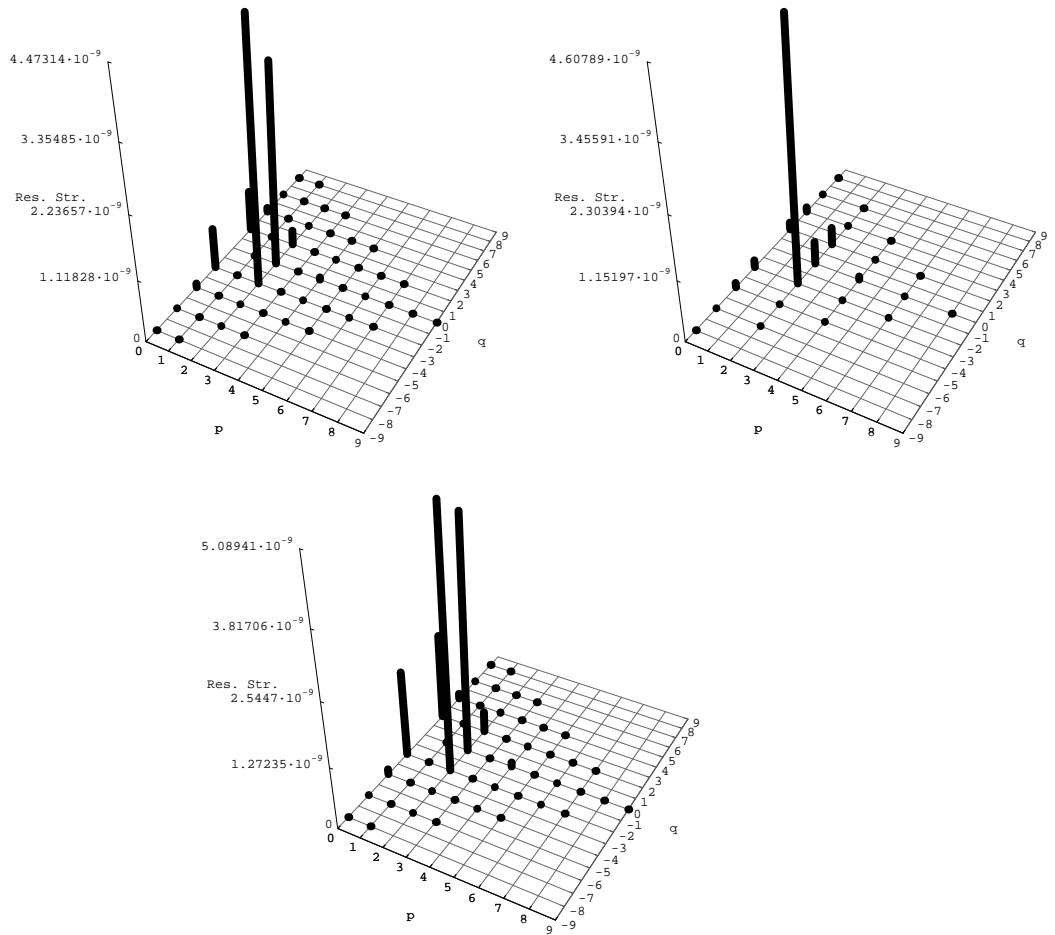
Figure 12: Resonance strengths for case 4.

Figures 17, 18 and 19 show that the tune shifts and footprints of case 6 are almost like adding up the corresponding pictures from cases 2 and 5. The resonance strengths are looking similar to those of case 2. This proves that the dominating fringe field effects are concentrated in the interaction regions, which has been showed to hold for other effects too, which are limiting the dynamic aperture.

The next two cases deal with the body errors. As mentioned in section 3, we have two possible signs for the uncertainty part of the errors. We use the same "average" seed for the random part in both cases. Case 7 is the (−) case,
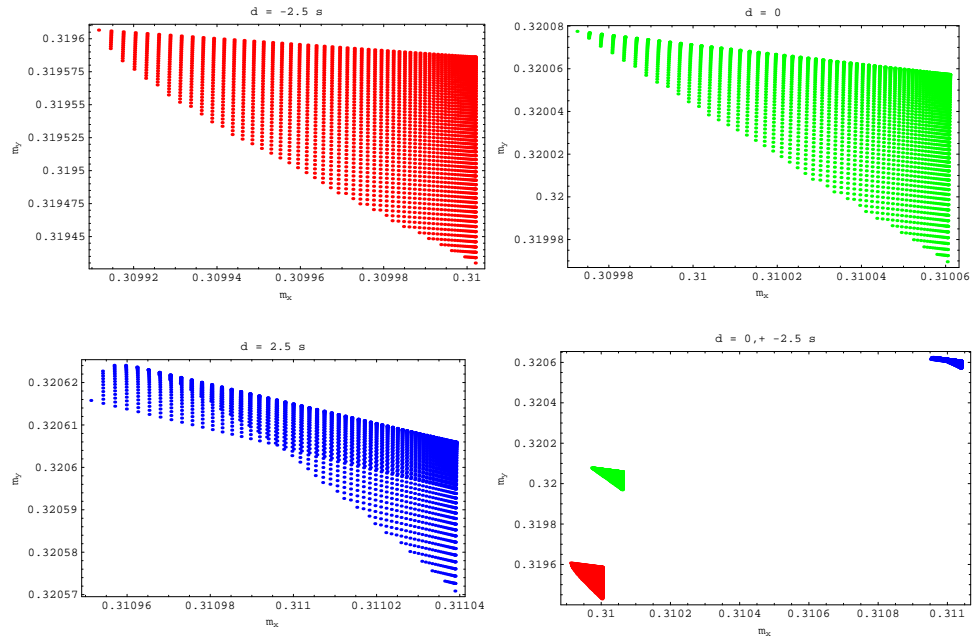
Figure 13: Tune footprints for case 5.
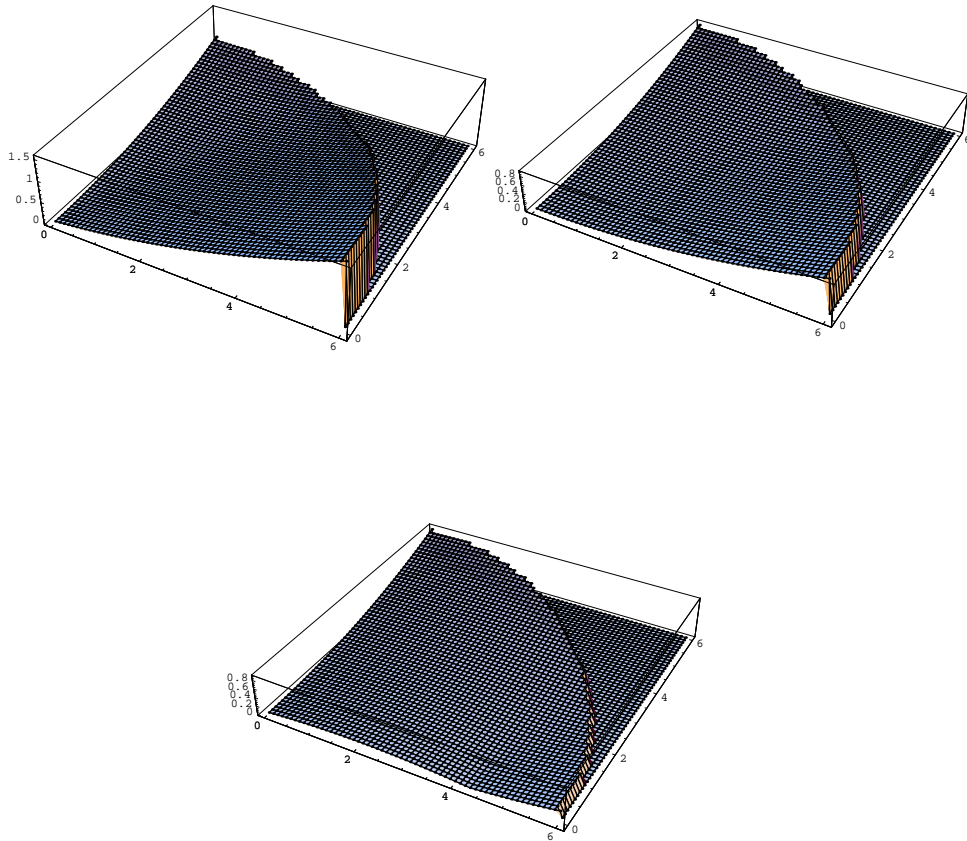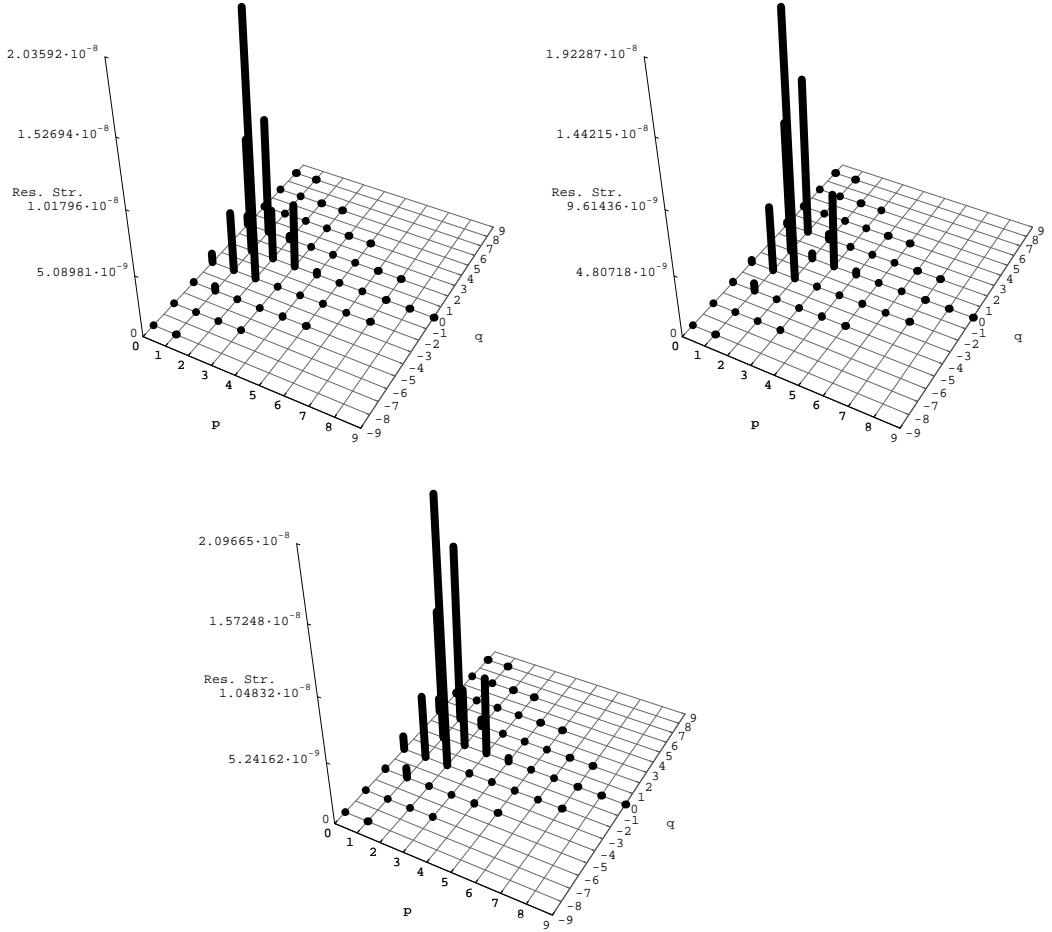

Figure 14: Tune shifts for case 5.

15

Figure 15: Resonance strengths for case 5.

and case 8 is the (+) case.

For case 7, figures 20, 21 and 22 show a little bigger tune shifts and footprints than for case 6, but still inside the safe region. The footprints are elongated and curved, and even overlapping for $\delta = -2.5\sigma_E$ and $\delta = 0$ respectively. On the other hand, the resonance strengths are amplified by 3 orders of magnitude. The new dominating resonance is $(0, 3)$. The resonances due to fringe fields and intrinsic nonlinearities are negligible.

Case 8 is the first situation where the maximum tune shift exceeds the acceptable level of 10^{-3} at 6σ (figure 24). See also figures 23 and 25.
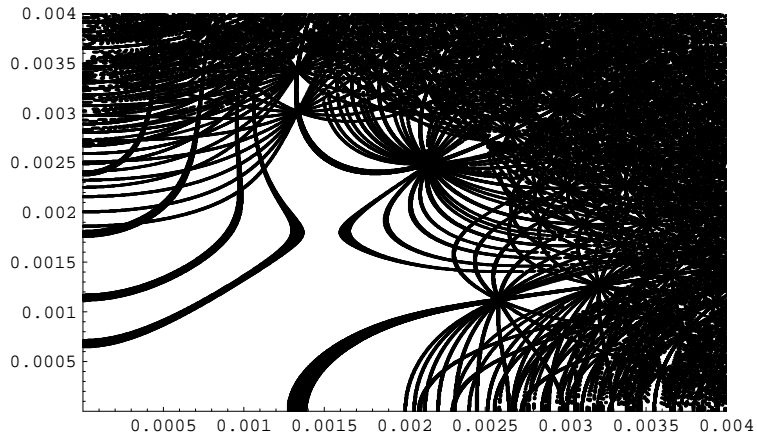
Figure 16: Resonance web for case 5, for $\delta = 0$.

Comparison of cases 7 and 8 proves that the systematic errors are important. However, notice that only a small fraction of the total particles, with predominantly horizontal initial amplitude, have tune shifts bigger than 10^{-3}. The other tune shifts are still bigger than in case 7, but within acceptable limits. The tune footprints are regular, triangle shaped, very elongated in one direction. The dominating resonance is still $(0, 3)$, with an important contribution from $(1, 2)$. Despite the fact that the tune shifts are bigger than in case 7, the magnitude of the resonance strengths are slightly smaller in case 8. Resonance structure is invariant with respect to energy.

The last to cases are the cases closest to reality from all the cases studied. We included the whole lattice at order 8, detailed fringe fields of the High Gradient Quadrupoles in the interaction regions and generic fringe fields for the rest of the ring, and body errors for interaction regions with the two possible signs. So, case 9 is actually cases 6 and 7 superimposed, and case 10 is cases 6 and 8 superimposed, respectively.

Figures 26 and 27 show that the tune footprints are only slightly distorted compared to case 7. The only case when the fringe fields clearly have a considerable effect is for $\delta < 0$ particles, but still inside acceptable limits. From figure
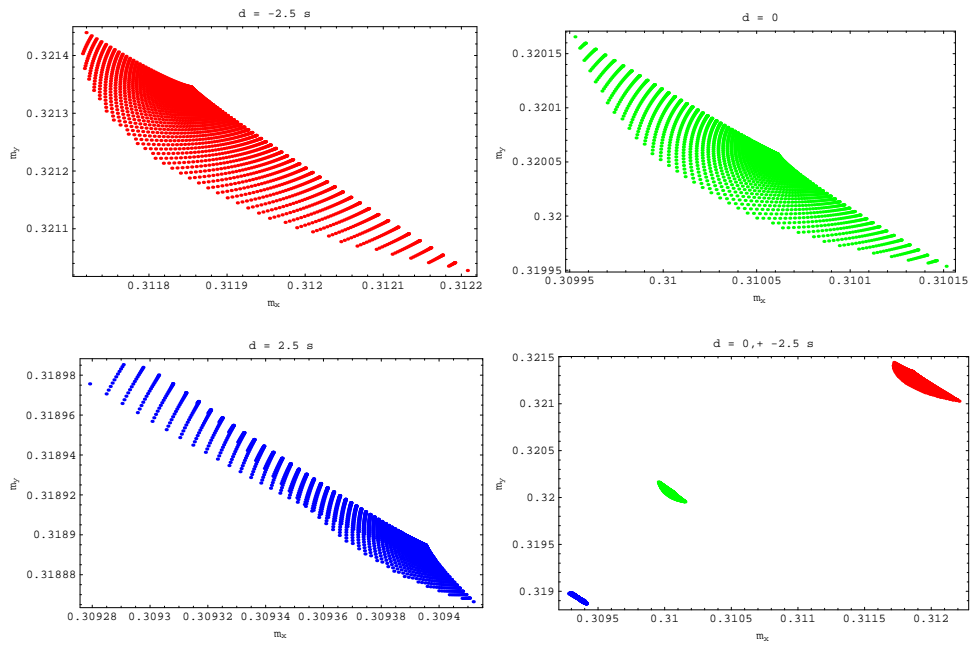
Figure 17: Tune footprints for case 6.
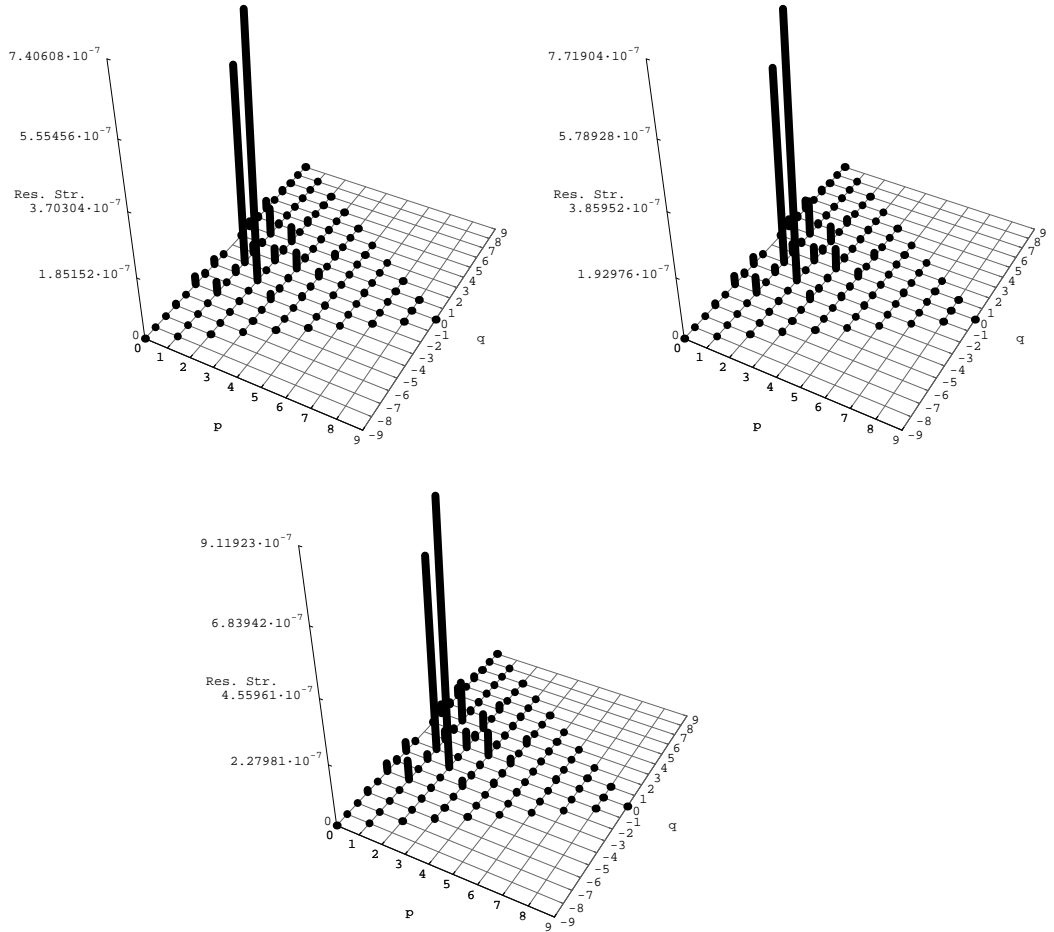

Figure 18: Tune shifts for case 6.

Figure 19: Resonance strengths for case 6.

28 it is obvious that the dominating resonances are excited by the body errors. Hence, the body errors dominate the fringe field effects. Note that the fringe fields alter the natural chromaticity (even change its sign). It is interesting to compare figures 29 and 16. The resonance channels in this case move much closer to the origin, inside the region occupied by the beam at target dynamic aperture. The chaotic boundary is around the target dynamic aperture. The thickest resonance channels remain $(1, -1)$, $(2, -2)$, $(3, -3)$, $(4, -4)$, $(0, 3)$ and $(1, 2)$.

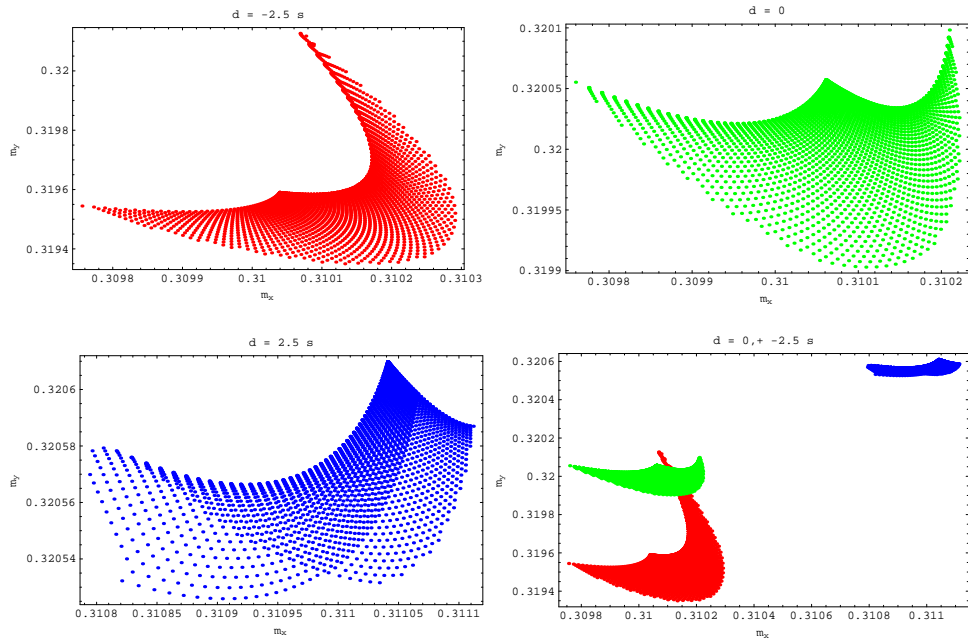Beside the fact that the tune shifts for $\delta < 0$ are much bigger in case 10,

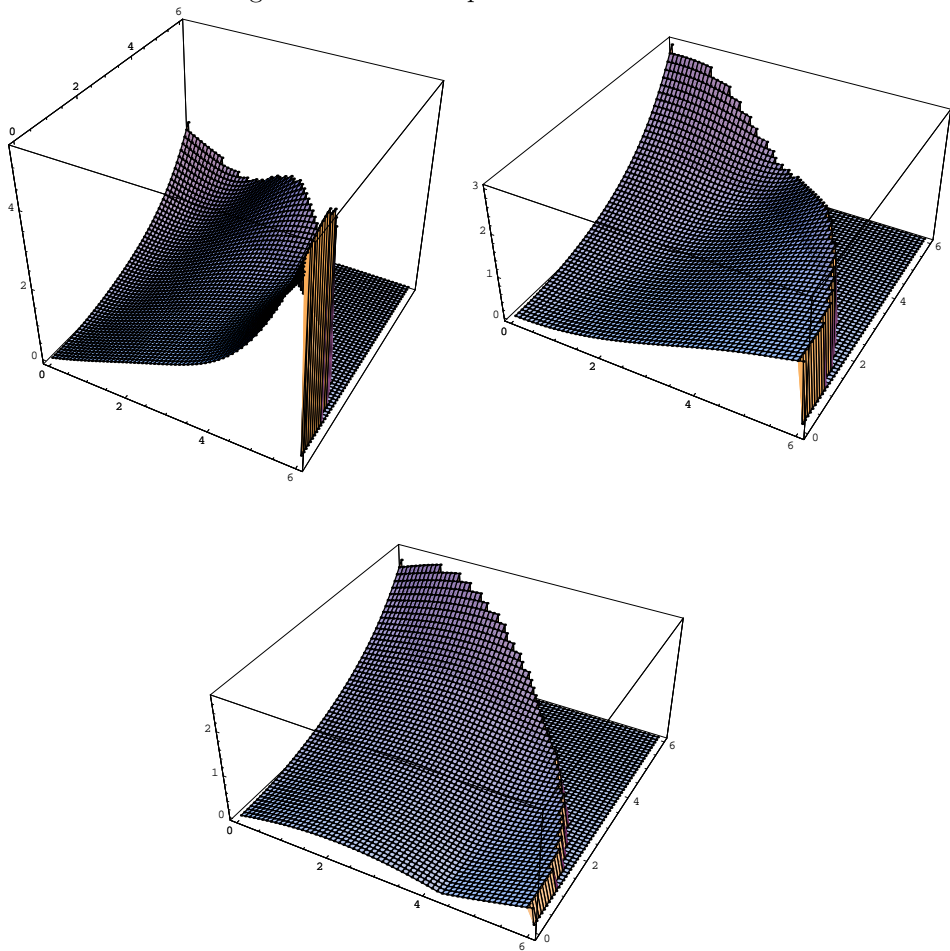Figure 20: Tune footprints for case 7.

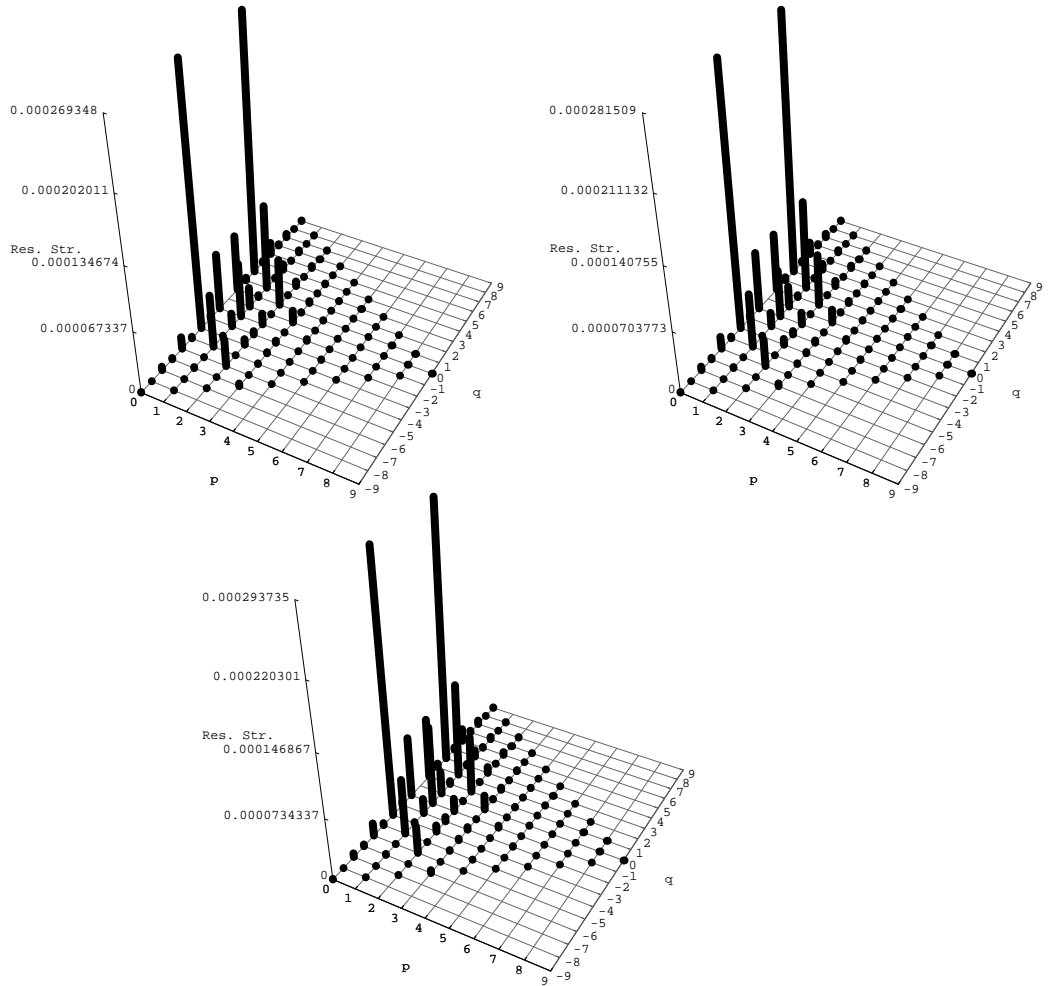Figure 21: Tune shifts for case 7.

Figure 22: Resonance strengths for case 7.

figures 30, 31 and 32 tell the same story as case 9. Again, the situation resembles case 8, only in this case the fringe fields have a little more influence than they had in case 9.

We computed the resonance webs for $\delta = -2.5\sigma_E$ and $\delta = 0$ to show a general conclusion, that the resonance web structure is essentially invariant with respect to energy. This is consistent with the invariance of resonance strengths with energy. From figure 33 results that the closest resonance lines are slightly farther away from the origin than in case 9. Also, in general the magnitudes of the resonance strengths increase with energy, and the resonance strengths of
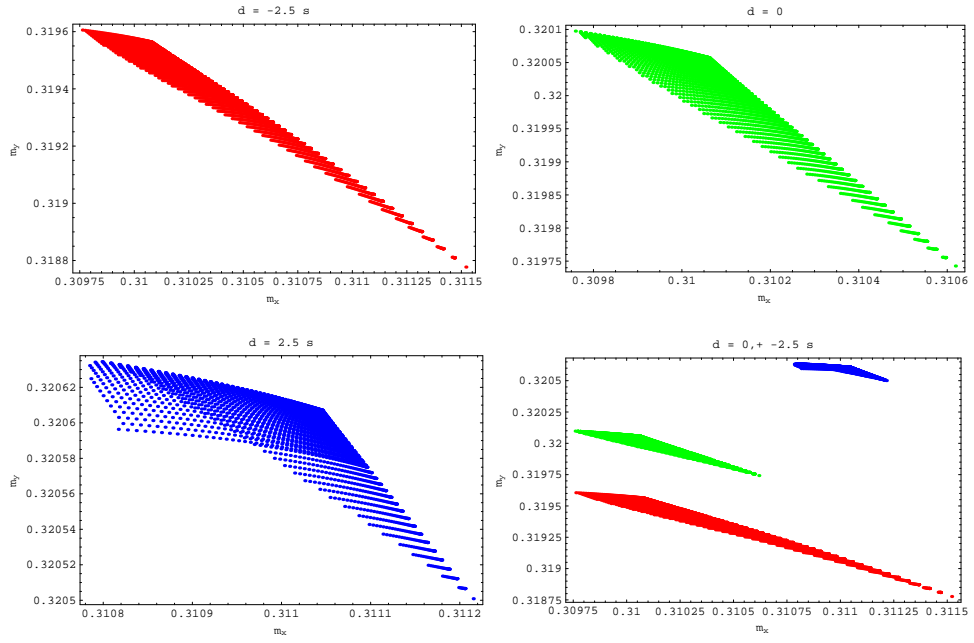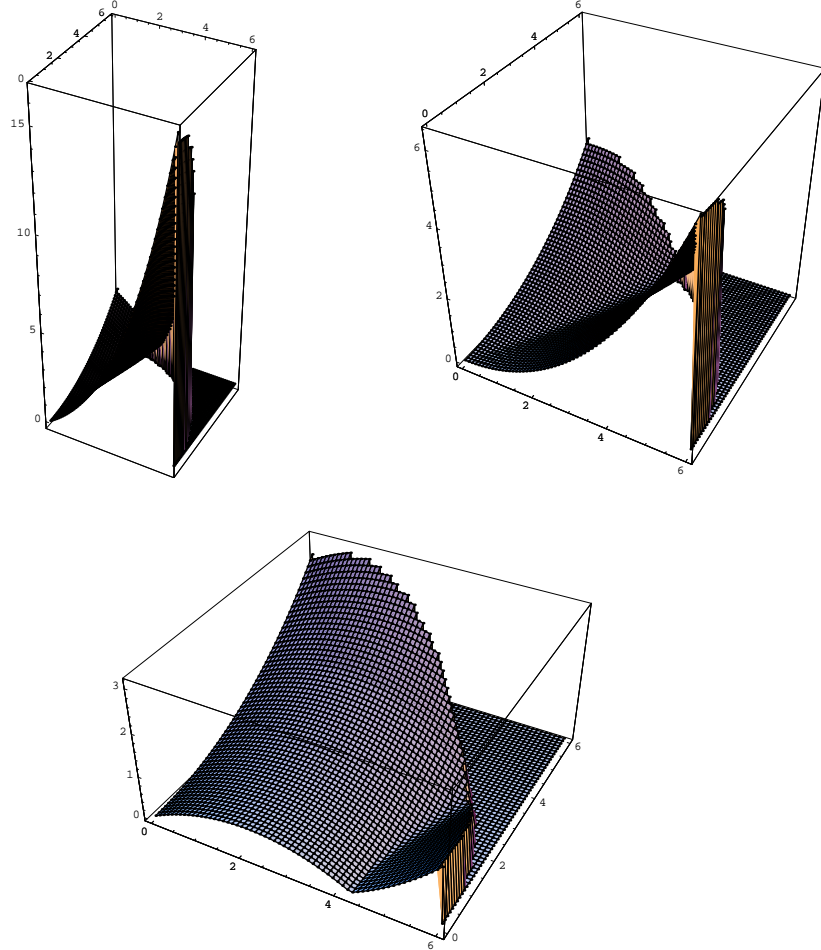
Figure 23: Tune footprints for case 8.
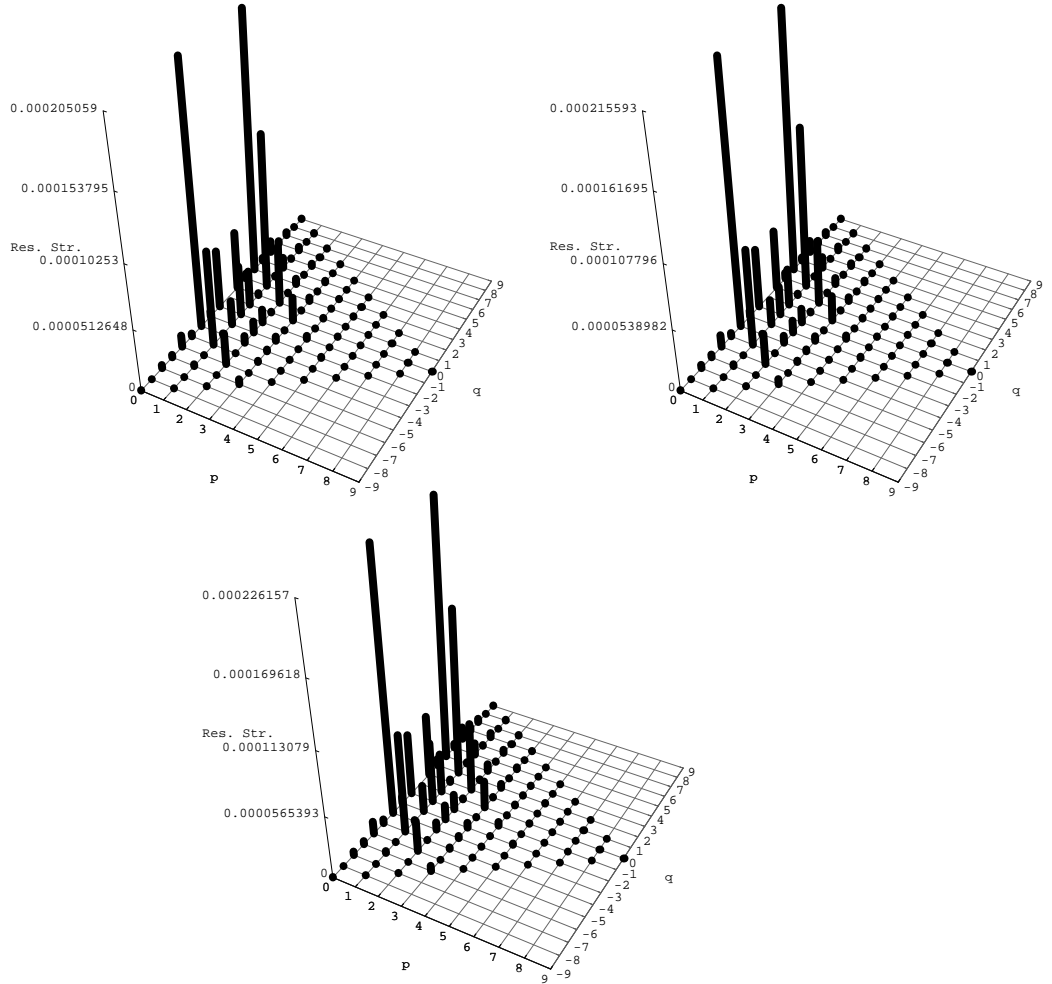

Figure 24: Tune shifts for case 8.

Figure 25: Resonance strengths for case 8.

case 10 are smaller than the resonance strengths of case 9. It is exactly the opposite for the tune shifts; the biggest are of case 10.

Finally, for cases 9 and 10 we computed the resonance strengths for $\delta = 0$ on a grid in action space, to identify the dominating resonances at different locations. See figure 34 for case 9 and figure 35 for case 10. Each picture represents a point on the grid, which extends from the origin (lower left picture) to $5 \cdot 10^{-4} m$, in steps of $10^{-4} m$ in both directions.

Due to lack of space, the pictures are so scaled down that it is not easy to read them. Therefore, we summarized the conclusions in figure 36.
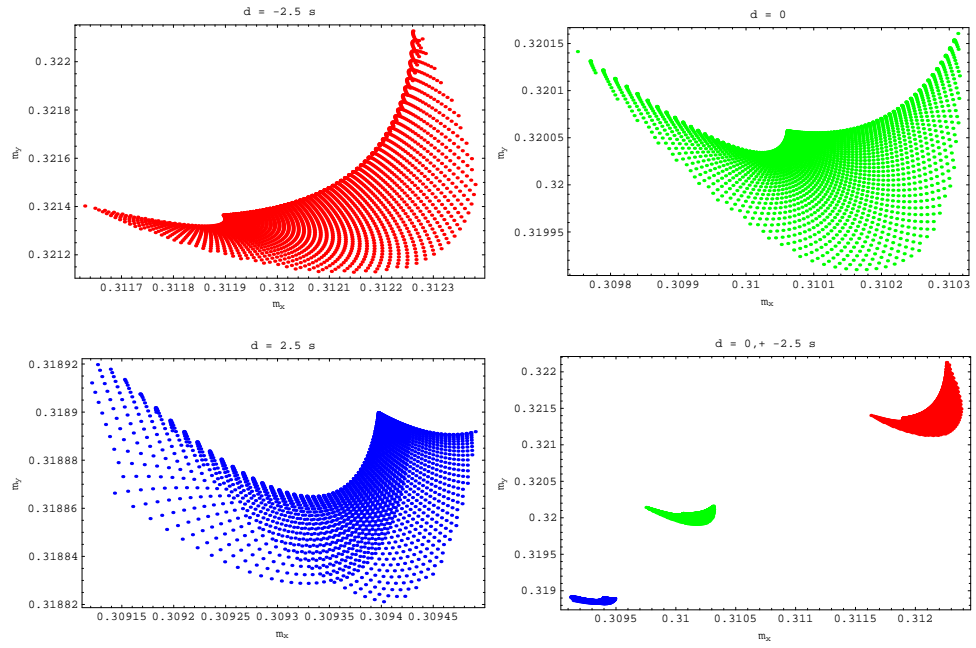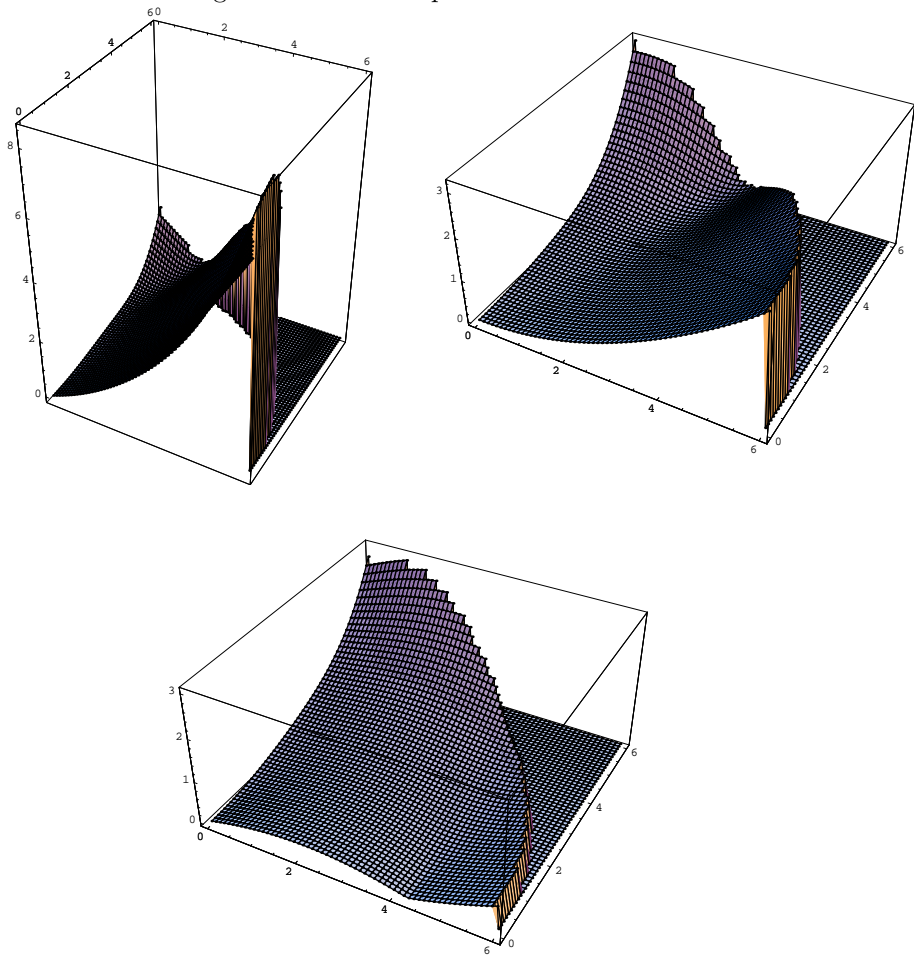
Figure 26: Tune footprints for case 9.

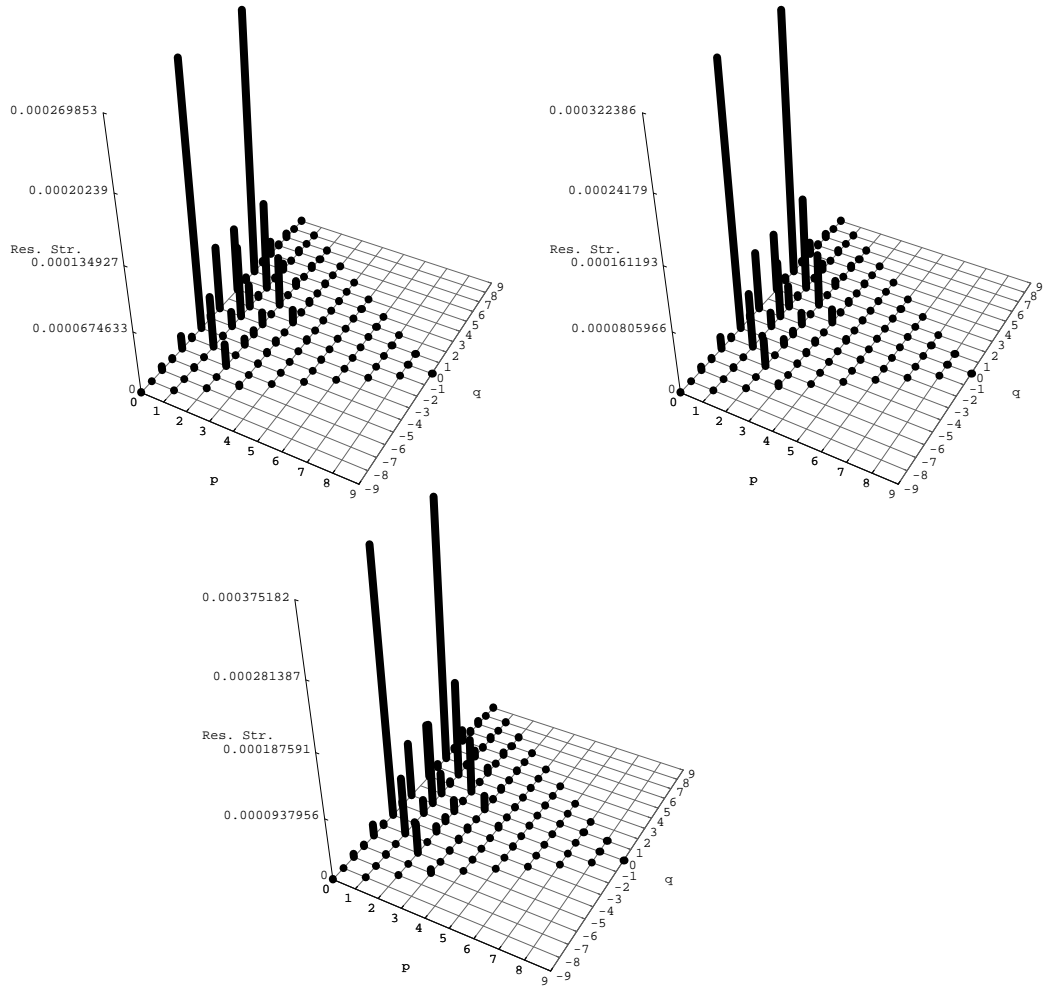Figure 27: Tune shifts for case 9.

24

Figure 28: Resonance strengths for case 9.

Obviously, $(0,3)$ is the dominating resonance in a major part of action space. For exactly horizontal motion $(3,0)$ is the dominating one, and there is a narrow region of predominantly horizontal motion for which $(1,-1)$ for case 9, and $(1,-1)$ or $(1,2)$ for case 10 are the dominating resonances, respectively. As we saw, the $(1,-1)$ is excited by the quadrupole component of the fringe fields. Hence, there is a small region where the dominating resonance is given by fringe fields. However, the magnitudes of the respective resonances are very small. Actually, the magnitude of the resonance strengths increase much more quickly in the vertical direction. Also, from the resonance web pictures results that the
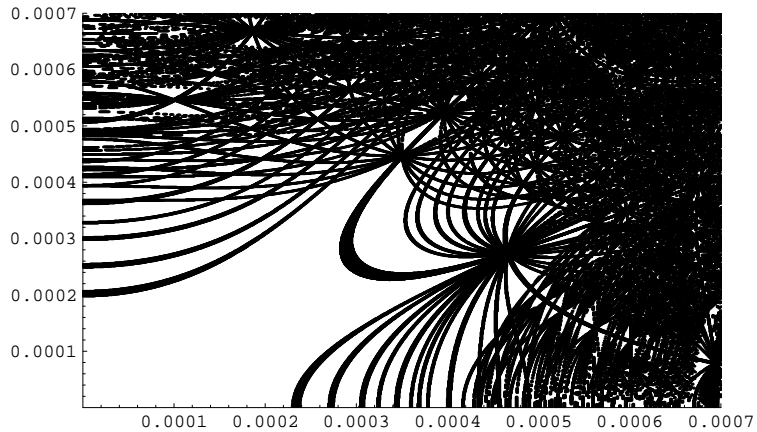
Figure 29: Resonance web for case 9, for $\delta = 0$.

closest resonance line to the origin is always along the vertical.

In a final paragraph we draw a few general conclusions. While the fringe fields generate important dynamical effects, as far tune shifts, footprints and resonance strengths are concerned, they are dominated by body errors. If there is a correlation between dynamic aperture and these quantities, than also the DA is determined by body errors. This is checked by tracking; the loss in DA due to fringe fields is at most $0.5\sigma_{x,y}$. On the other hand, the DA cannot be correlated exactly with both tune shifts and resonance strengths. This can be seen from the fact that we do not get the largest tune footprints for the case with the largest resonance strengths and vice versa. However, roughly it is correlated with both indicators. The resonance strength and resonance web results are consistent in the sense that resonance lines closer to the origin give larger resonance strengths. Regarding the shape of fringe fields, we could conclude that the exact shape does not matter. However, intrinsically the fringe field effects are not very important for the LHC, and for other situations, like the proposed Muon Collider, where the relative importance of the fringe fields are greater, it can be expected that the shape of fringe field will be also important. For the LHC, most of fringe field effects are generated by the High Gradient Quadrupoles.
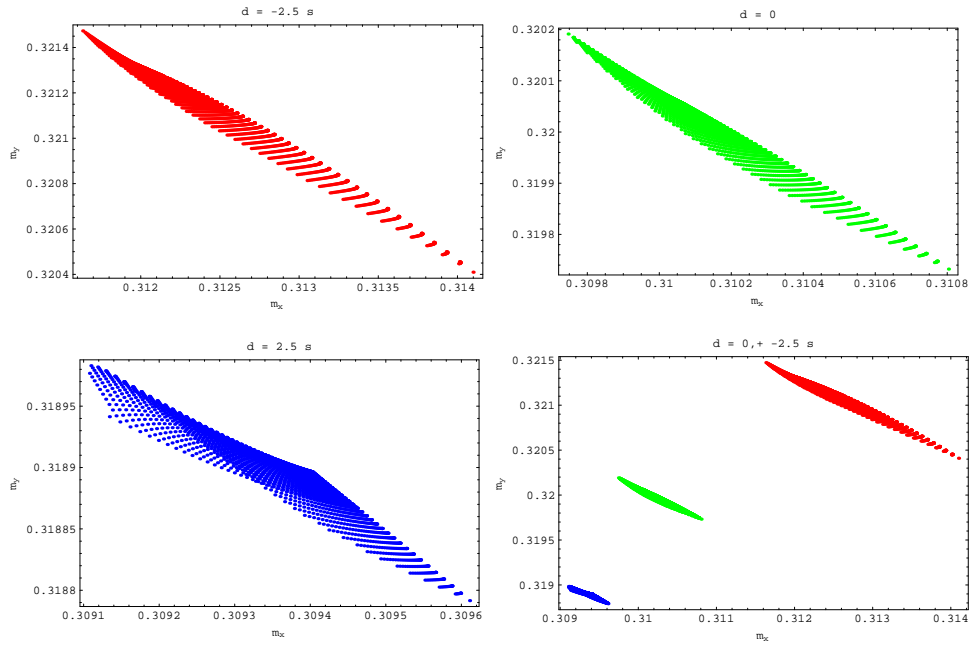
26

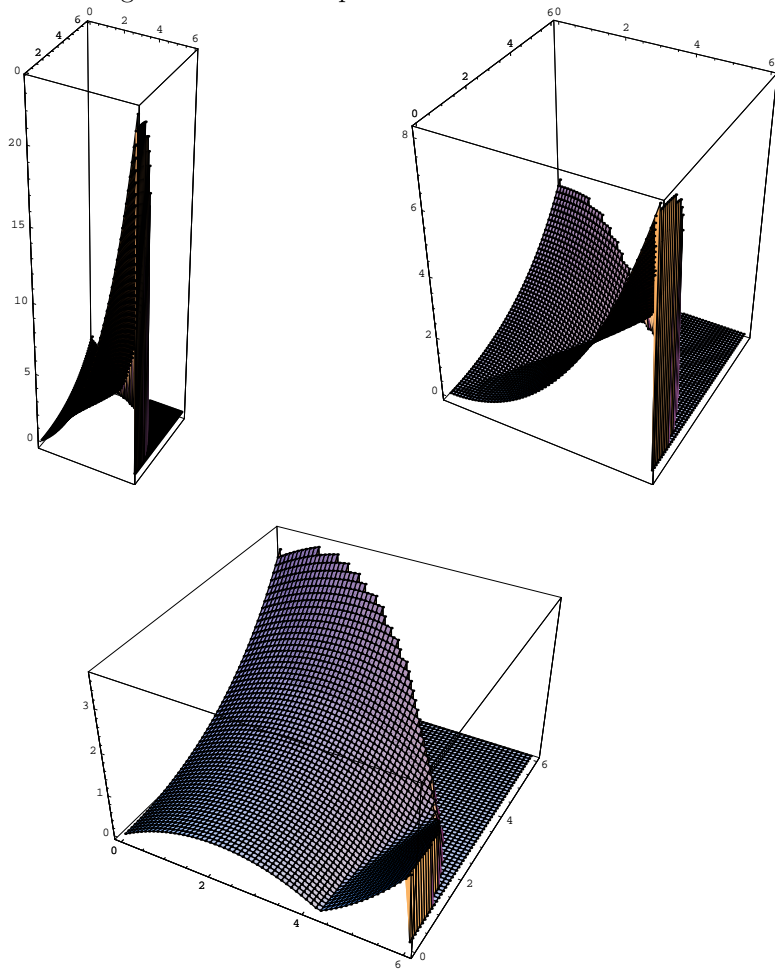Figure 30: Tune footprints for case 10.

Figure 31: Tune shifts for case 10.
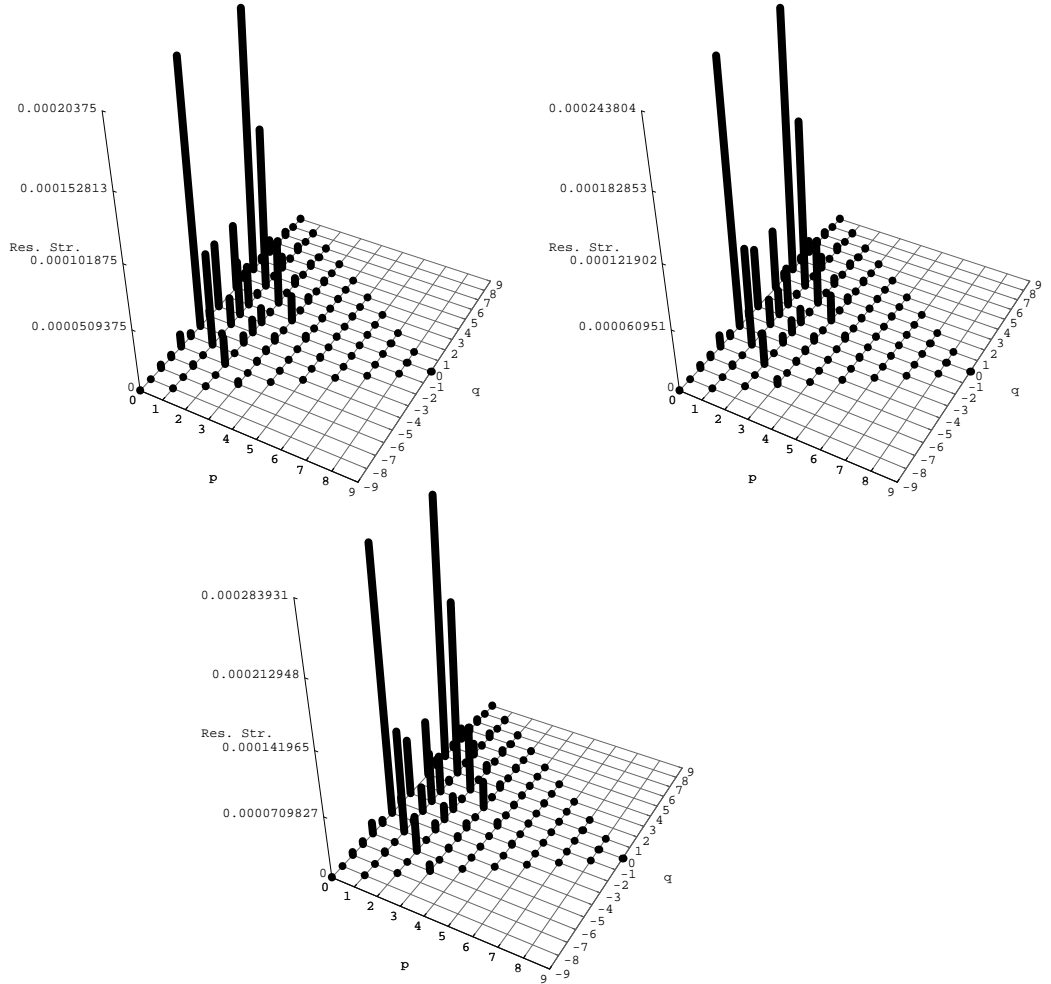
Figure 32: Resonance strengths for case 10.

The energy dependence of the tunes show that in general tune shifts are maximized for predominantly horizontal motion for $\delta < 0$, and as energy increases, the maximum decreases and shifts towards predominantly vertical motion. For on-energy particles the tune shifts are approximately symmetric with respect to diagonal, with minimums attained around the diagonal. This implies that, if the tune shifts are correlated with the DA, the estimation of the DA using only on-energy particles launched along the diagonal will result in an overestimation of the DA. Resonance strengths and resonance webs are roughly invariant with respect to energy. However, a marginal increase of the resonance strengths with

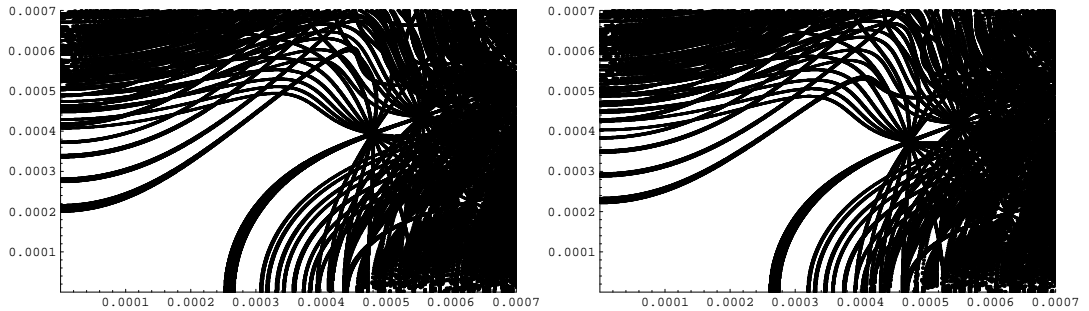Figure 33: Resonance web for case 10, for $\delta = -2.5\sigma_E$ and $\delta = 0$.

energy is usually observed. The trend for the tune shifts is exactly opposite. In some cases, a substantial decrease of the footprints is observed as energy increases. Over a large portion of action space the dominant resonance is $(0, 3)$. The resonance strengths increase in magnitude faster in the vertical direction. The magnitudes of the dominating resonances in the strip of predominantly horizontal motion are much smaller than in the rest of action space. The biggest jump in the magnitudes is observed at around $2 \cdot 10^{-4}$ along the vertical, which by coincidence or not is the location of the closest resonance line to the origin in the resonance web pictures.

References

[1] B. Erdelyi, M. Berz, and M. Lindemann. Differential algebra based magnetic field computations and accurate fringe field maps. in preparation, 1999.

[2] J.-P. Koutchouk. The LHC dynamic aperture. In *Proceedings PAC '99*, New York, 1999. AIP.

[3] M. Berz. Differential algebraic formulation of normal form theory. In *M. Berz, S. Martin and K. Ziegler (Eds.), Proc. Nonlinear Effects in Accelerators*, page 77, Publishing, 1992. IOP.

[4] R. Bartolini and F. Schmidt. Normal form via tracking of beam data. Technical Report LHC Project Report 132, CERN, 1998.

[5] K. Makino and M. Berz. COSY Infinity version 8. *Nucl. Instr. Meth. A*, 427:338–343, 1999.
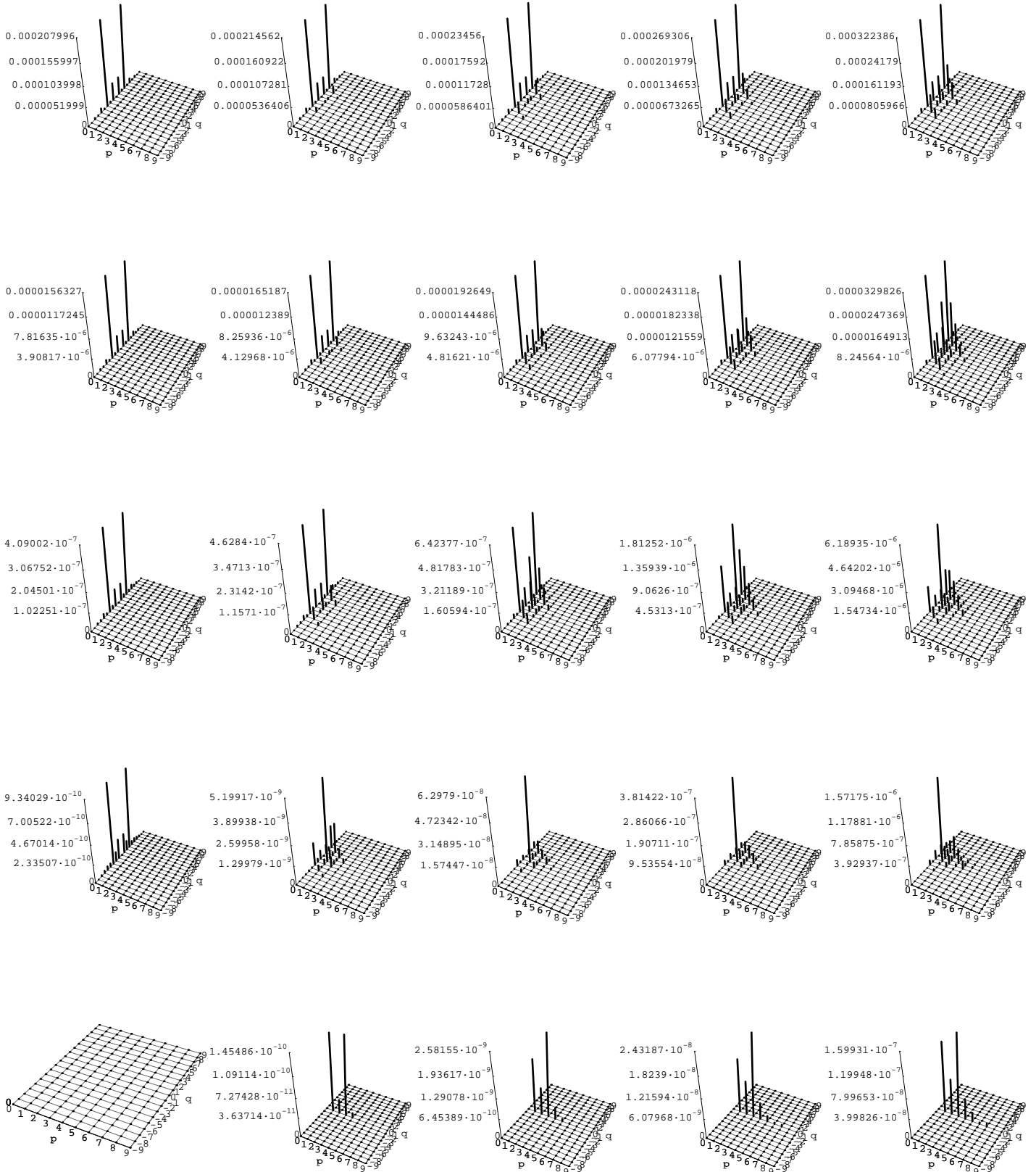
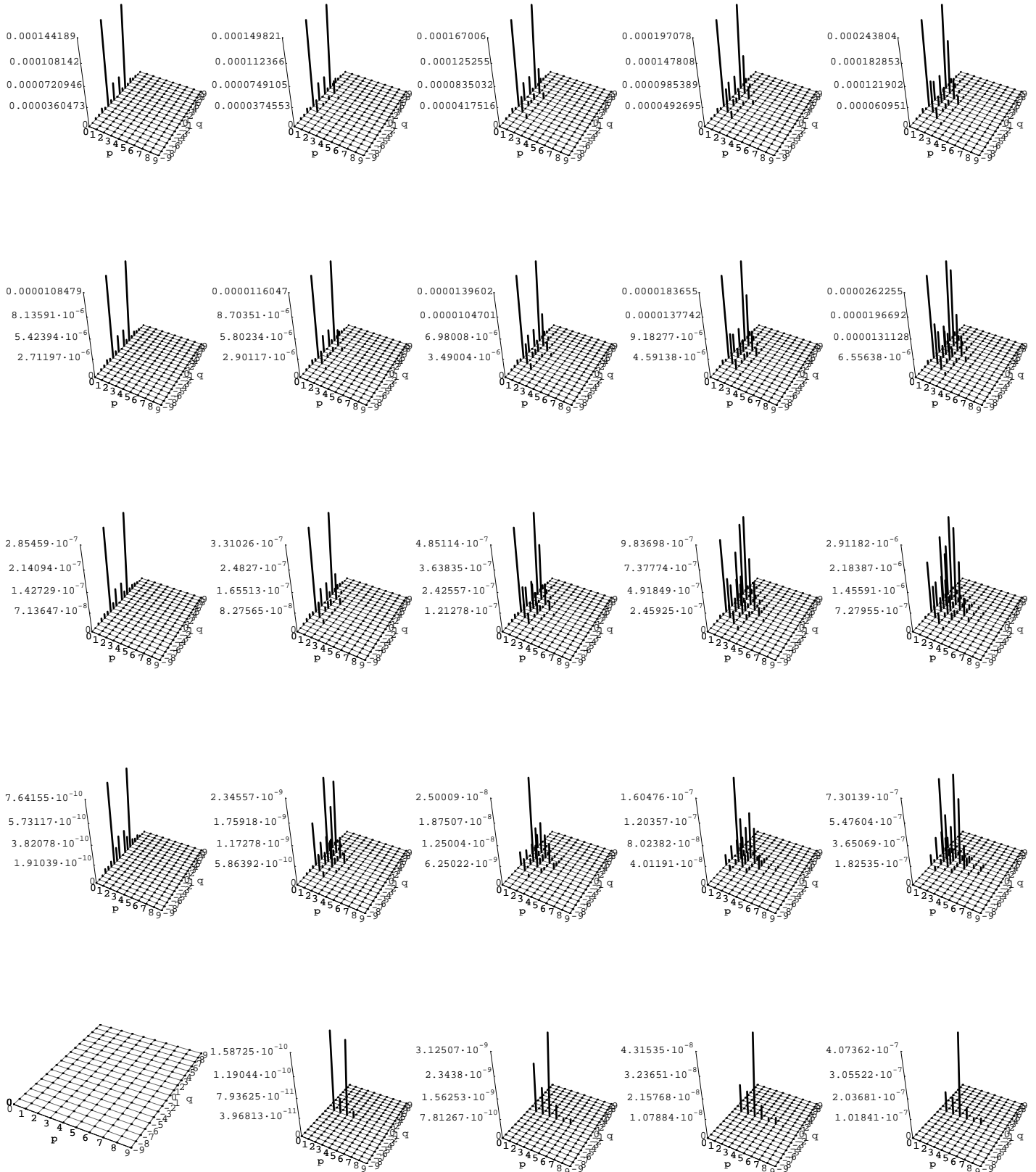Figure 34: Resonance strengths on a grid in action space for case 9.

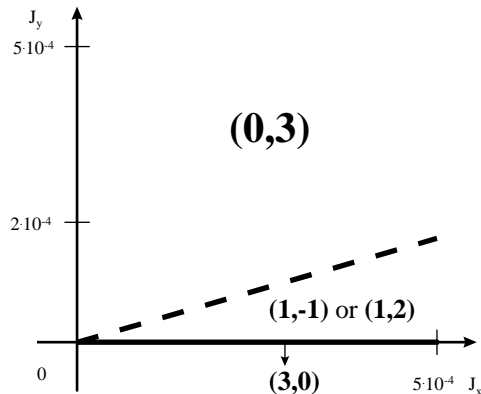Figure 35: Resonance strengths on a grid in action space for case 10.

Figure 36: Dominating resoances for cases 9 and 10.

[6] G. Sabbi. Magnetic field analysis of HGQ coil ends. Technical Report TD-97-040, Fermilab, 1997.

[7] L. Bottura, A. Jain, D. McChesney, F. Pilat, G. Sabbi, and J. Wei. Summary of US-LHC magnet database workshop. Technical Report RHIC/AP/160, BNL, Long Island, New York, 1998.

[8] W. Wan. *Theory and Applications of Arbitrary-Order Achromats.* PhD thesis, Michigan State University, East Lansing, Michigan, USA, 1995. also MSUCL-976.

[9] K. Makino. *Rigorous Analysis of Nonlinear Motion in Particle Accelerators.* PhD thesis, Michigan State University, East Lansing, Michigan, USA, 1998.

A Map Transformations Under Orientation Flips

Sometimes, orientation changes of particle optical elements in an accelerator lattice are used as a mean to compensate or correct nonlinearities, improving the characteristics of the accelerator. One specific case is the LHC HGQs in the interaction regions [7]. We will study the problem of knowing the map of an element in a "default" orientation, what kind of transformations are necessary in order to obtain the maps of the "flipped" elements. Specifically, we need 3 different (similarity) transformations on the map, corresponding to mirroring the "default", or "forward" element with respect to a plane. Here we use W. Wan's nomenclature [8]. Mirroring the forward element with respect to the $x-y$ plane gives the "reversed" element, with respect to the $y-z$ plane gives the "switched" element, and with respect to the $x-z$ plane gives the "upside-down" element. In [8] it is explained how to obtain the map of mirrored elements knowing the map of the forward element.

The map of the reversed element in the (x, a, y, b, l, δ) symplectic basis is given by

$$M_R = R \circ M^{-1} \circ R$$

where

$$R = \begin{pmatrix} 1 & 0 & 0 & 0 & 0 & 0 \\ 0 & -1 & 0 & 0 & 0 & 0 \\ 0 & 0 & 1 & 0 & 0 & 0 \\ 0 & 0 & 0 & -1 & 0 & 0 \\ 0 & 0 & 0 & 0 & 1 & 0 \\ 0 & 0 & 0 & 0 & 0 & -1 \end{pmatrix}$$

is an involution: $R \circ R = I$, I the identity, that is $R^{-1} = R$. M is the map of the forward element.

Analogously, the switched map can be obtain from the forward map as

$$M_S = S \circ M \circ S$$

with

$$S = \begin{pmatrix} -1 & 0 & 0 & 0 & 0 & 0 \\ 0 & -1 & 0 & 0 & 0 & 0 \\ 0 & 0 & 1 & 0 & 0 & 0 \\ 0 & 0 & 0 & 1 & 0 & 0 \\ 0 & 0 & 0 & 0 & 1 & 0 \\ 0 & 0 & 0 & 0 & 0 & 1 \end{pmatrix}$$

possessing similar properties as R: $S \circ S = I$, $S^{-1} = S$.
The last one is the upside-down transformation

$$M_U = U \circ M \circ U$$

with

$$U = \begin{pmatrix} 1 & 0 & 0 & 0 & 0 & 0 \\ 0 & 1 & 0 & 0 & 0 & 0 \\ 0 & 0 & -1 & 0 & 0 & 0 \\ 0 & 0 & 0 & -1 & 0 & 0 \\ 0 & 0 & 0 & 0 & 1 & 0 \\ 0 & 0 & 0 & 0 & 0 & 1 \end{pmatrix}$$

Again, $U \circ U = I$, $U^{-1} = U$.

It is well known that an element satisfying midplane symmetry is invariant under the upside-down transformation. Next, we will show under what conditions an element is invariant with respect to reversion.

The conditions can be deduced from Hamilton's equations. In the case of planar reference orbit, no electric fields, and s-independent magnetic fields (in which case the fields are derivable from the vector potential component A_s, and $A_x = A_y = 0$), the most general Hamiltonian [9] is invariant under the transformation R. Moreover, the canonical equations of motion and hence the map of a such an element in invariant under the transformation R_α, where α means that it inverts the sign of the independent variable s, when acting on a map.

$$R_\alpha \circ M = M \circ R_\alpha$$

In the Lie Algebraic notation, the map can be written in the form

$$M = e^{-\Delta s :H:}$$

where $:H:$ is the Poisson bracket operator attached to the Hamiltonian of the system. Hence, $\alpha(M) = M^{-1}$, since $:H:$ commutes with itself.

Inserting it in the invariance relation we obtain

$$
\begin{aligned}
R \circ M^{-1} &= M \circ R \\
&\Downarrow \\
M &= R \circ M^{-1} \circ R
\end{aligned}
$$

Comparison with the map of the reversed element gives the result

$$M_R \equiv M$$

In the specific case of the LHC, 180 degree rotations of quadrupoles around the y axis are performed. This transformation is equivalent to mirroring the forward element with respect to the $x - y$ plane, and then with respect to the $y - z$ plane. In other words, we obtain a "combined" element as the combination of the reversed and switched element. Finally, we can identify the combined element's map with the map of the "opposite" quadrupole's map. For details, see [7].

Now we can show that the combined element is unique, that is the reversed and switched, and switched and reversed elements have the same map.

1) Reversed and Switched

$$M_C = S \circ \left(R \circ M^{-1} \circ R \right) \circ S$$

34

2) Switched and Reversed

$$
\begin{aligned}
M_C^{'} &= R \circ (S \circ M \circ S)^{-1} \circ R \\
&= R \circ S \circ M^{-1} \circ S \circ R \\
&= S \circ R \circ M^{-1} \circ R \circ S \\
&= S \circ \left(R \circ M^{-1} \circ R\right) \circ S \\
&= M_C
\end{aligned}
$$

We used the fact that $S^{-1} = S$, and being diagonal matrices $[R, S] = R \circ S - S \circ R = 0$. Actually, all the individual transformations commute due to the fact that they are generated by diagonal matrices.

So we have an easy procedure to compute the maps of arbitrary "opposite" elements from the "default" ones. Moreover, the map approach is valid for arbitrary field configurations, including detailed fringe fields and compositions of several maps. In the case of $s-$independent elements, we obtain simplifications due to invariance under reversion. This property is relevant for the implementation of the body errors, in which case we can get the map of the opposite quadrupole by switching the default map. Of course, in the case of detailed fringe field maps, one needs to perform the reversion too.

To compare the above results with the rules for multipole sign changes due to orientation changes [7], we derive the results based on field multipole expansion. Suppose that eq.6 gives the multipole expansion in the default reference frame.

$$
B_y + i B_x = \sum_n (b_n + i a_n) (x + iy)^n \tag{6}
$$

As a contrast with the map methods, this formula and hence the derivation is valid only for s-independent elements, or the integrated strengths in the end regions. In the same way, we assume that the expansion in the opposite frame is

$$
B_{y'} + i B_{x'} = \sum_n \left(b_n^{'} + i a_n^{'}\right) \left(x^{'} + iy^{'}\right)^n
$$

First, the reversion consists of the following transformations

$$
\begin{aligned}
x^{'} &\to x \qquad y^{'} \to y \qquad z^{'} \to -z \\
B_{x'} &\to -B_x \qquad B_{y'} \to -B_{y'}
\end{aligned}
$$

Inserting them in the expansion gives

$$
B_y + i B_x = \sum_n - \left(b_n^{'} + i a_n^{'}\right) (x + iy)^n
$$

Comparing coefficients with eq.6 we obtain

$$
\begin{aligned}
b_n^{'} &\equiv -b_n \\
a_n^{'} &\equiv -a_n
\end{aligned}
$$

The switching can be cast in a similar way to correspond to the following transformations

$$
\begin{aligned}
x' &\to -x & y' &\to y & z' &\to z \\
B_{x'} &\to B_x & B_{y'} &\to -B_{y'}
\end{aligned}
$$

$$
-B_y + iB_x = \sum_n \left(b_n^{'} + ia_n^{'} \right) (-x + iy)^n
$$

Taking the complex conjugate of the above expression we arrive to

$$
\begin{aligned}
-B_y - iB_x &= \sum_n \left(b_n^{'} - ia_n^{'} \right) (-x - iy)^n \\
B_y + iB_x &= \sum_n (-1)^n \left(-b_n^{'} + ia_n^{'} \right) (x + iy)^n
\end{aligned}
$$

Comparing coefficients with eq.6 we obtain

$$
\begin{aligned}
b_n^{'} &\equiv (-1)^{n+1} b_n \\
a_n^{'} &\equiv (-1)^n a_n
\end{aligned}
$$

The upside-down transformation can be expressed as

$$
\begin{aligned}
x' &\to x & y' &\to -y & z' &\to z \\
B_{x'} &\to -B_x & B_{y'} &\to B_{y'}
\end{aligned}
$$

$$
B_y - iB_x = \sum_n \left(b_n^{'} + ia_n^{'} \right) (x - iy)^n
$$

Taking the complex conjugate expression we arrive to

$$
B_y + iB_x = \sum_n \left(b_n^{'} - ia_n^{'} \right) (x + iy)^n
$$

which gives the relation between multipole coefficients

$$
\begin{aligned}
b_n' &\equiv b_n \\
a_n' &\equiv -a_n
\end{aligned}
$$

Finally, we get the rule for the combined (opposite) element as the commutable product of the reversion and switching transformation

$$
\begin{aligned}
b_n' &\equiv (-1)^n b_n \\
a_n' &\equiv (-1)^{n+1} a_n
\end{aligned}
$$

in agreement with [7]. Direct calculation shows that the above results are in complete agreement with [7] for every case, after the polarity is changed following the transformation such that the fundamental term remains positive; in case it is necessary.

As a conclusion, the above map manipulations based on the matrices R, S, and U form a complete set of commutable transformations to perform any flip scenario, including arbitrary s-dependent fields, and maps of composed elements. All the necessary map computations, compositions and inversions are easily performed in the Differential Algebra based code COSY Infinity.